Universität Leipzig

Fakultät für Physik und Erdsystemwissenschaften

Evaluation of cross-talk effect on the retrieval of atmospheric particle extinction coefficient profiles by using a rotational-Raman lidar

Bachelorarbeit

Vorgelegt von:

Nathan Skupin
Matrikelnummer: 3757683
nathan.skupin@gmail.com

Erstgutachter: Dr. Cristofer Jimenez
Zweitgutachter: Prof. Dr. Andreas Macke

Leipzig, den 3. September 2024

Abstract

Remote sensing technologies like Lidar and Radar significantly enhance atmospheric data acquisition. However, the quality of data from these multi-channel systems is limited by both theoretical and practical challenges. One major issue is the separation of multiple signals, typically managed through optical filters. Unfortunately, these filters are not perfect—neither their transmission nor reflectance reaches zero at specific wavelengths, leading to spectral leakage or cross-talk. This phenomenon causes deviations in the measured signal compared to the actual incoming signal.

In Raman Lidar systems, where the elastic signal significantly exceeds the inelastic signals, gray filters are used to attenuate the elastic channel before it reaches the detectors. This introduces both real and effective cross-talk, which are related through the characterizing Lidar constants of the involved channels. Polly_1v2, a Lidar system that utilizes both rotational- and vibrational-Raman channels, exemplifies this issue, with the rotational-Raman channel being particularly susceptible to cross-talk due to its shorter Raman shift, complicating spectral seperational through the deployed optical filters. By analyzing atmospheric properties calculated from these channels, the individual cross-talk values can be extracted.

The thesis introduces a practical method to correct the cross-talk effect and examines the observations from two campaigns, as well as its correspondence with the actual transmission curves of the used filters. The findings contribute to understanding the impact of cross-talk on the retrieval of extinction coefficient profiles and highlight the challenges associated with the method.

Contents

1 Introduction

Since the invention of the laser in 1960, a wide array of fields including manufacturing, medicine, and research have embraced its applications (Maiman, 1960). Notably, the development of Lidar (Light Detection and Ranging) technology has revolutionized range detection measurements by utilizing short laser pulses to measure the time it takes for light to travel to a scattering target and back (U. Wandinger, 2005a).

The initial uses of Lidar, from satellite tracking to the mapping of the moon's surface, relied on reflections from solid surfaces (Lehr, 1966; Woodward and Walters, 1971). However, the technology's application in atmospheric data acquisition evolved significantly with cloud-ranging experiments, utilizing scattering processes on small atmospheric particles (Collis, 1965). Atmospheric Lidar technology has diversified into several specialized types (U. Wandinger, 2005a):

- Raman Lidar: This type captures signals from elastic and inelastic scattering processes of specific molecules, providing data on atmospheric parameters like extinction and backscatter coefficients.

- Differential-absorption Lidar: By emitting light with two closely spaced wavelengths around an absorption line, the differential optical attenuation can be measured.

- Fluorescence Lidar: Utilizing electronic excitations to detect traces of metallic atoms in the mesopause region.

- Doppler Lidar: Employs the Doppler effect to measure velocities of moving particles or air masses, useful for detecting rain and wind speeds.

The accuracy of Lidar data depends heavily on the quality of its components. A stable, linearly polarized, monochromatic laser with narrow bandwidth and low divergence is required. Photomultiplier Tubes (PMTs) may struggle to differentiate between simultaneous photon arrivals (Acharya, Sharma, and Chandra, 2004), and background radiation can degrade data quality. A critical source of error lies in signal separation, managed through optical filters, such as beam splitters and interference filters, which differentiate signals based on wavelength and polarization. Non-ideal behavior in these components corresponds to incomplete signal reflection and transmission, leading to spectral leakage or cross-talk. Cross-talk effect, characterized by the relative intensity of unwanted signals contributing to the measured signal of each channel, is particularly noticeable when separating signals of similar wavelengths and with large intensity differences (Yang et al., 1997).

The portable Lidar system Polly_1v2 (Althausen et al., 2009) emits laser light at 532 nm. It uses 5 detection channels: the elastic channel for all polarization planes, referred to as the total elastic channel, along the elastic channels for cross- and co-polarization, the vibrational-Raman channel detecting light at 607 nm and the rotational-Raman channel detecting light at 530 nm (TROPOS, 2024a).

For such systems, the impact of cross-talk extends beyond just signal interference; it affects the retrieval of atmospheric quantities like the extinction coefficient. Making use of the fact that every additional inelastic channel produces an additional particle extinction coefficient profile, one can be used as a reference, while the other is adjusted for its cross-talk. This correction process involves the measured elastic signal, whose intensity is typically attenuated through neutral density filters before detection, resulting in varying effective cross-talk values. However, multiplying by the Lidar constant ratio, which can be extracted from the respective Lidar equations (U. Wandinger, 2005a), yields the real cross-talk value for the elastic attenuated backscatter, providing a balanced evaluation of the effect and enabling a comparison to the theoretical transmission curves of the relevant filters.

This thesis aims to evaluate the impact of cross-talk on the retrieval of atmospheric particle extinction coefficients for periods with particularly strong elastic return such as cloud cases, using the Raman Lidar Polly_1v2. Data from the Leipzig and Tirana campaigns will be used to assess the reliability and temporal consistency of the methods developed (TROPOS, 2024b). Practical challenges such as environmental effects and other influencing factors will also be discussed.

The structure of this thesis is organized as follows:

- *Chapter 2* discusses the Lidar system components and the theoretical framework underlying their operation.
- *Chapter 3* will delve into Raman Lidar specifics, including the retrieval of extinction and backscatter coefficient with a deeper physical discussion on inelastic molecular scattering.
- *Chapter 4* explains the relevant components of the optical setup used to separate the backscattered light, and the mathematics underlying the cross-talk effect.
- *Chapters 5 through 7* will present the methodology, results and discussion for the determination of the cross-talk parameters and the Lidar constant ratio, respectively.
- *Chapter 8* concludes with a summary of findings and implications for future research.

2 Principle Lidar Setup

Lidar technology utilizes light in the form of a pulsed laser to measure profiles of backscattered signals at variable distances. This chapter explores the fundamental setup of a Lidar system, divided into its core components: the emission of light, interactions within the atmosphere, and the detection mechanisms. It concludes with a mathematical framework for understanding how Lidar accurately captures atmospheric data. The majority of this content is drawn from the foundational work *Introduction to Lidar* by Wandinger (2005).

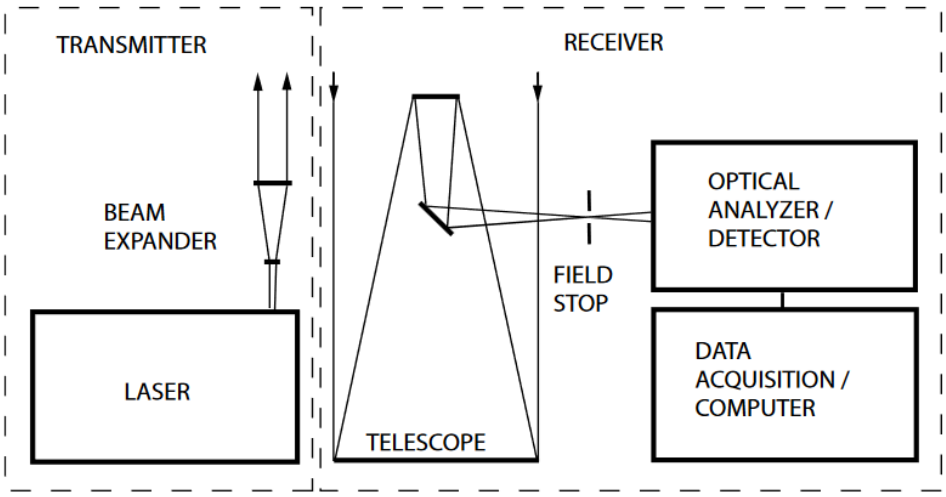

Figure 1: Lidar setup from U. Wandinger, 2005a

2.1 Transmitter Components

The transmitter consists of the laser and the beam expander, illustrated in Figure 1.

Lasers operate on the principle of population inversion, where atoms in the laser medium are excited to a higher energy state through a process known as pumping. When these atoms return to their ground state, they emit photons that stimulate the emission of more photons, leading to a cascade effect. An optical resonator, acting as a closed cavity, amplifies the stimulated emission until a Q-switch lets the photons escape, producing a high-intensity laser pulse of a few meters in length, ensuring precise timing (Baars, Engelmann, et al., 2023).

While the Nd:YAG laser is a commonly used laser device in today's Lidar systems, emitting linearly polarized monochromatic light with a wavelength of 1064 nm, other laser types such as Ti:Sapphire and CO_2 lasers are also used depending on the application (Bass, 2010). Frequency doubling and tripling

within Nd:YAG lasers allow for the generation of wavelengths of 532 nm and 355 nm, respectively, which are useful for different types of atmospheric measurements (Baars, Engelmann, et al., 2023).

The beam expander, consisting of two optical lenses, extends the Gaussian-shaped beam radius and reduces its divergence to about 0.1 mrad, resulting in a relatively constant intensity profile across various heights.

2.2 Scattering Processes

The atmosphere is composed of molecules like nitrogen, oxygen, and water vapor, as well as larger particles known as aerosols which contribute to the formation of cloud droplets. The interaction of light with these particles results in various scattering processes, which can be broadly categorized into elastic and inelastic types.

Elastic scattering maintains the wavelength of the incident light. It includes Rayleigh-, Mie-, and optical scattering, each differentiated by the relative size of the particles compared to the wavelength of light and the directional distribution of the scattered light. Rayleigh scattering occurs when light induces a dipole on small particles, causing an oscillation at the same frequency as the incident light, ultimately emitting radiation of the same wavelength (Placzek, 1934). Mie scattering, which occurs when light interacts with spherical particles that are comparable in size to its wavelength, results in an asymmetrical scattering distribution. Optical scattering, observed in larger particles such as cloud droplets, is strongly asymmetrical and can maintain the polarization of scattered light (Hahn, 2009).

In contrast, inelastic scattering results in a frequency shift or change in wavelength due to energy transfer with the scatterer, such as phonon interaction, molecular excitations, or electronic excitations, also known as Raman scattering. Stokes-Raman-Scattering occurs when the photon loses energy to the scatterer, whereas Anti-Stokes-Raman-Scattering occurs when it gains energy from the particle. These processes are further discussed in the *Raman Lidar* chapter.

2.3 Receiver Components

As the Lidar beam travels through the atmosphere, a fraction of the light is scattered back towards the system. This backscattered light is collected by a telescope positioned adjacent to the beam expander, which captures photons within a fixed field of view (FOV). The overlap between the FOV and the laser beam increases with height, and the resulting overlap function $O(z)$ describes this dependency.

The received light passes through optical filters, such as beam splitters and interference filters, which separate it based on its wavelength and polarization. These filters are not perfect and can introduce cross-talk, which will be examined in detail in the chapter on *Optical Filters*. The separated photons are then counted by photomultiplier tubes (PMTs), which convert these counts into an electrical or digital signal. PMTs, however, have a finite relaxation time, meaning they cannot count two photons arriving simultaneously. This introduces inaccuracies in the count numbers, a phenomenon known as the dead-time effect (Hopkins, 1991).

2.4 Lidar Equation

The backscattering process varies with height, affecting the time it takes for photons to return to the receiver, highlighted in Figure 2. The scattering height is calculated using the equation

$$R = \frac{c\Delta t}{2}, \tag{1}$$

where c is the speed of light and Δt is the time difference between the light being emitted and detected.

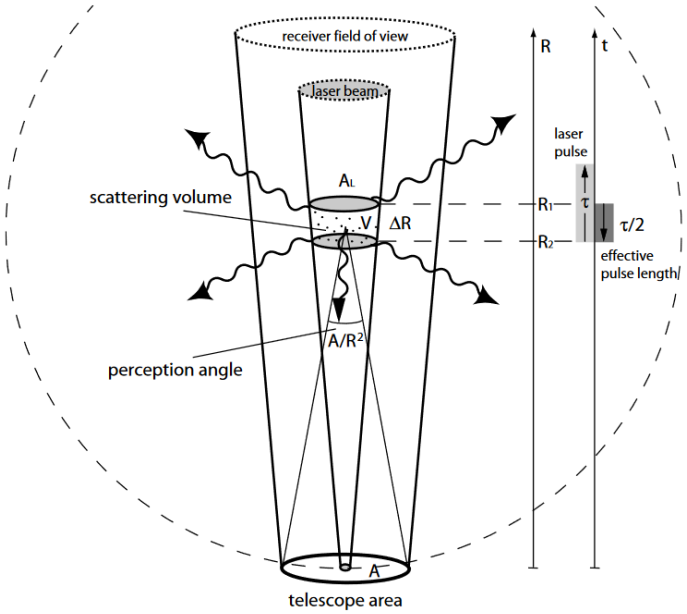

Figure 2: Lidar geometry from (U. Wandinger, 2005a)

The received signal strength from a specific height is governed by the Lidar

equation:

$$P_\lambda(z) = P_0 \frac{O(z)}{z^2} C_s(\lambda) \beta_\lambda(z) T_{\lambda_0}(z) T_\lambda(z) \tag{2}$$

where P_0 is the power of a single laser pulse of the incident light and $O(z)$ represents the overlap function. The system constant $C_s(\lambda)$ encompasses the efficiency of the Lidar system, including the transmission and detection coefficients. It accounts for the attenuation introduced by beam splitters, gray filters, and the transmission of interference filters. A detailed discussion on these components is provided in the *Optical Filters* chapter. The range-correction term z^{-2} accounts for the shrinking perception angle with increasing height as the backscattered light needs to fall within this angle to be captured by the telescope, demonstrated in Figure 2.

The backscatter coefficient β quantifies the amount of light scattered back towards the receiver. Since the laser light interacts with both air molecules and particulate matter, each contribute to the overall backscatter factor:

$$\beta = \beta^{\text{mol}} + \beta^{\text{par}} \tag{3}$$

The transmittance T represents the fraction of light that hold out against scattering and absorption along its path. This term takes the form

$$T_\lambda(z) = \exp\left(- \int_0^z \alpha_\lambda(r) dr \right) , \tag{4}$$

where the extinction coefficient α encapsulates the combined effect of molecular and particle extinction

$$\alpha = \alpha^{\text{mol}} + \alpha^{\text{par}} . \tag{5}$$

The transmittance appears twice to account for the way to the backscattering source and back.

Implementing the lidar equation requires consideration of additional factors that can affect measurement accuracy: The duration of the laser impulse τ is non-zero. This introduces a limitation on the spatial resolution of the system, as it is not possible to differentiate signals from within a vertical distance less than $\frac{c\tau}{2}$. This distance represents the minimum resolvable height interval, below which individual measurements cannot be distinguished.

Background radiation, particularly significant during daylight measurements, must be accounted for to ensure accurate signal detection. This involves measuring the background radiation separately and subtracting this value from the actual measurements:

$$P_\lambda^{\text{corrected}}(z) = P_\lambda(z) - P_\lambda^{\text{bg}} \tag{6}$$

3 Raman Lidar

Raman Lidar systems utilize channels specifically designed to detect inelastic scattering, each characterized by distinct frequency shifts. This chapter explores the underlying physics of these shifts, the calculation of scattering cross sections, and the subsequent signal intensity of backscattered light. A thorough understanding of these aspects is crucial for evaluating the feasibility of measuring various inelastic signals. This exploration sets the foundation for developing mathematical models to retrieve atmospheric particle extinction and backscatter coefficient profiles.

3.1 Raman Shifts

Raman spectroscopy involves measuring the wavenumber shift between incident and scattered light, known as the Raman shift:

$$\Delta\tilde{\nu} = \tilde{\nu}_0 - \tilde{\nu} = \frac{1}{\lambda_0} - \frac{1}{\lambda}\,, \tag{7}$$

which corresponds to the energy transfer to or from the scatterer, expressed by

$$\Delta E = E'' - E' = hc\Delta\tilde{\nu}\,, \tag{8}$$

where h is Planck's constant, c is the speed of light(U. Wandinger, 2005b).

Raman lidar systems measure the frequency-shifted light, primarily resulting from molecular vibrational and rotational transitions. The molecular behaviour is governed by quantum mechanics, which dictates discrete energy levels for molecules.

Molecular vibrations occur due to the movement of atoms within a molecule around a potential minimum at the equilibrium bond distance r_0. The bonding can be thought of as a linear restoring force $F(r) = -k(r - r_0)$, akin to Hook's law (Wilson, Decius, and Cross, 1980). For diatomic molecules, this results in a harmonic oscillator model, leading to the quantized energy states (Allen et al., 1990):

$$E_v^{\text{vib}} = hc\omega(v + 1/2), \quad v = 0, 1, 2, \ldots \tag{9}$$

where v is the vibrational quantum number and ω is the vibrational wavenumber. For anharmonic oscillators, an additional correction term is included (Allen et al., 1990):

$$E_v^{\text{vib}} = hc\left[\omega(v + \frac{1}{2}) - \omega\chi(v + \frac{1}{2})^2\right] \tag{10}$$

with the anharmonicity constant χ.

For diatomic molecules, the rotational energies can be modeled using the rigid rotor approximation (Banwell and McCash, 1994):

$$E_J^{\text{rot}} = hcBJ(J+1), \quad J = 0, 1, 2, \ldots \tag{11}$$

where J is the rotational quantum number and B is the rotational constant. Centrifugal stretching due to molecular rotation necessitates a correction, leading to (Banwell and McCash, 1994)

$$E_J^{\text{rot}} = hc\left[BJ(J+1) + DJ^2(J+1)^2\right] \tag{12}$$

where D is the centrifugal distortion constant. B and D can be expressed as

$$B = \frac{\hbar}{4\pi cI} \text{ and } D = \frac{\hbar^3}{4\pi cI^2 r^2 k} \tag{13}$$

with I being the moment of inertia of the molecule.

For combined vibrational-rotational energy levels, modified constants B_v and D_v account for changes in inertia due to vibrational motion (Banwell and McCash, 1994; U. Wandinger, 2005b). The combined energy states are:

$$E_{v,J}^{\text{vib-rot}} = hc\left[\omega\left(v+\frac{1}{2}\right) - \omega\chi\left(v+\frac{1}{2}\right)^2 + B_v J(J+1) - D_v J^2(J+1)^2\right]. \tag{14}$$

In practical applications $D_v = D_e$ and B_v can be approximated linearly as $B_e - \alpha_e(v+\frac{1}{2})$, where B_e and D_e describe constants at the equilibrium position and α_e describes the rotational-vibrational interaction constant (Lovas, Tiemann, et al., 2005).

For triatomic molecules a more complex mathematical model is neccessary to account for the increased number of interacting vibrational and rotational modes, which is explained by the Triatomic Spectral Database (Lovas, Coursey, et al., 2003). For example, the linear molecule CO_2 has one rotational axis and one Raman-active vibrational mode, while water molecules have three rotational axis and three Raman-active modes. However, for low energy transitions, Equation 14 can still be used (Lovas, Coursey, et al., 2003).In Table 1, the vibrational and rotational constants for various atmospheric molecules are summarized.

Furthermore, Equation 8 becomes

$$\Delta\tilde{\nu} = \frac{1}{hc}\left(E_{v'',J''}^{\text{vib-rot}} - E_{v',J'}^{\text{vib-rot}}\right), \tag{15}$$

where v' and J' denote the initial quantum numbers and v'' and J'' the quantum

Molecules	ω	$\omega\chi$	B_e	α_e	D_e
N_2	2358.57	14.324	1.99824	0.017318	5.76×10^{-6}
O_2	1580.19	11.98	1.43768	0.0159	4.84×10^{-6}
CO_2	1333	-	0.39021	-	-
H_2O	3657 (O-H s.) 3756 (O-H a.) 1595 (H-O-H)	-	27.877 (A) 14.512 (B) 9.285 (C)	-	-

Table 1: Vibrational and Rotational Constants for N_2, O_2 (*NIST Chemistry WebBook* 2023), H_2O and CO_2 (*NIST Computational Chemistry Comparison and Benchmark Database* 2022), in units of [cm^{-1}].

numbers after the transition.

Possible Raman transitions are categorized by the selection rules: $\Delta v = 0, \pm 1$ and $\Delta J = 0, \pm 2$, as long as overtones are prohibited (U. Wandinger, 2005b). Specifically:

- $\Delta v = 0, \Delta J = 0$ corresponds to Rayleigh scattering
- $\Delta v = 0, \Delta J = \pm 2$ corresponds to pure rotational-Raman scattering
- Combined vibrational-rotational transitions are categorized into:
  - S-branch: $\Delta v = \pm 1, \Delta J = +2$
  - Q-branch: $\Delta v = \pm 1, \Delta J = 0$ (pure vibrational-Raman scattering)
  - O-branch: $\Delta v = \pm 1, \Delta J = -2$

Using the equipartition theorem, the energy associated with each degree of freedom can be estimated by $\frac{1}{2}k_bT$. For atmospheric temperatures typically not exceeding 300 K , which corresponds to $\tilde{\nu} = 104\,\mathrm{cm}^{-1}$, most molecules are in the vibrational ground state, in contrast to the rotational levels which follow the Boltzmann distribution law. Table 2 provides the Raman shifts for the most probable transitions, calculated with the molecular constants from Table 1.

The calculated rotational Raman shifts for N_2, O_2 and H_2O align with the spectra shown in Figure 3 utilizing Equation 7.

Besides molecular excitations, other inelastic scattering processes are also noteworthy. According to molecular orbital theory (MOT), electrons occupy energy levels determined by the bonding atoms in a molecule, which means electronic excitations can occur. The frequency shifts for the first electronic excitation energies, which satisfy all selection rules, are as follows:

Molecular Transitions	N_2	O_2	CO_2	H_2O
Rot-Stokes [cm^{-1}]	91.45	77.11	38.24	167.13
Rot-Anti-Stokes [cm^{-1}]	-75.56	-65.71	-35.12	-92.85
Vib-S-Branch [cm^{-1}]	2418.67	1630.00	-	-
Vib-Q-Branch [cm^{-1}]	2328.02	1553.75	1333	3657
Vib-O-Branch [cm^{-1}]	2253.11	1488.77	-	-

Table 2: Raman shifts for different types of rotational and vibrational transitions for various molecules. For H_2O the symmetric O-H vibrational mode and the rotational energy of the C-axis was used. The initial rotational state was set to the peak of the Boltzmann distribution at $J' = \left\lfloor \sqrt{\frac{104\text{cm}^{-1} \cdot f}{B_e}} \right\rfloor$, while $v' = 0$. Calculated by the author.

- N2: 50203 cm^{-1} (*NIST Chemistry WebBook* 2023)
- O2: 49793.28cm^{-1} (*NIST Chemistry WebBook* 2023)
- H_2O: 56500cm^{-1} (Aschi et al., 2005)
- CO_2: 61000cm^{-1} (Buenker et al., 2000)

These shifts require UV light for excitation, making them less relevant for Lidar applications.

Phonons, which describe collective excitations of a periodic arrangement of atoms or molecules, are phenomena almost exclusively observed in solid matter. For instance, ice, which can adopt various crystal structures, commonly exists as hexagonal ice (Ih) in the atmosphere. Raman spectroscopy of ice (Abe and Shigenari, 2011) reveals a phonon-related Raman shift at 231 cm^{-1}, compareable to rotational-Raman shifts.

3.2 Cross Sections

The interaction probability of light and a scatterer is based on its scattering cross section σ, which can be thought of as the effective area the scatterer inhabits in the light's direction. Lidar applications particularely rely on the Rayleigh and backscattering cross sections. The Rayleigh cross section after Elterman, 1968 is calculated by

$$\sigma^{\text{Ray}}(\lambda) = \frac{8\pi^3(n(\lambda)^2 - 1)^2}{3\lambda^4 N_s^2} \cdot \frac{6 + 3\delta}{6 - 7\delta}\,, \tag{16}$$

where $\delta = 0.00279$ is the depolarization factor, N_s the molecular number concentration for standart conditions, and the refractive index n is calculated with Edlen's expression (Baars, Engelmann, et al., 2023):

$$n(\lambda) = 1 + 10^{-8}\left(8342.13 + \frac{2406030}{130 - \lambda^{-2}[\mu\text{m}^2]} + \frac{15997}{38.9 - \lambda^{-2}[\mu\text{m}^2]}\right) \tag{17}$$

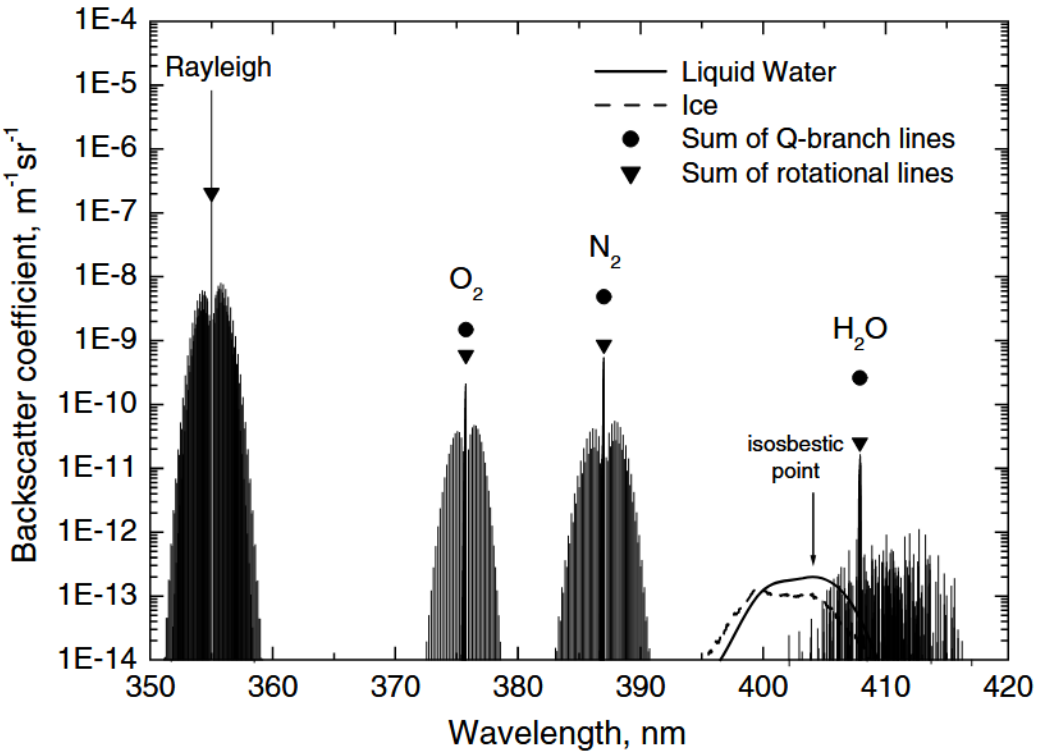

Figure 3: Raman backscatter spectrum of the atmosphere for a laser wavelength of 355nm at normal pressure and 300K from U. Wandinger, 2005b.

The backscattering cross section, describes the differential cross section $\frac{d\sigma}{d\Omega}$ at 180°, corresponding to the intensity of light scattered back towards the receiver.

The ability of a molecule to undergo scattering is influenced by its polarizability constants: the mean polarizability a, the anisotropic polarizability γ, and their derivatives with respect to vibrational coordinates, a' and γ'. The ability to induce an electric dipole on a molecule or particle with an electromagnetic wave is the polarizability. Based on the polarizability theory by Placzek, 1934, the differential cross-sections for various scattering processes can be calculated. The following equations are based on the works of U. Wandinger, 2005b in *Raman Lidar*.

The Rayleigh scattering cross section, which includes contributions from both elastic and inelastic processes, is given by

$$\left(\frac{d\sigma}{d\Omega}\right)^{\text{Ray}} = \frac{\pi^2}{\epsilon_0^2}\tilde{\nu}_0^4\left(a^2 + \frac{7}{180}\gamma^2\right) . \tag{18}$$

with the vacuum perimivity ϵ_0. For pure rotational-Raman scattering the dependency is of similar nature:

$$\left(\frac{d\sigma}{d\Omega}\right)^{\text{rot}} = \frac{\pi^2}{\epsilon_0^2}\tilde{\nu}_0^4\left(\frac{7}{60}\gamma^2\right) . \tag{19}$$

As the zero-point energy

$$b_v = \sqrt{\frac{h}{8\pi^2 c\omega}} \tag{20}$$

of the vibrational modes are above the thermal energy, the Boltzmann distribution is included for Stokes- and Anti-Stokes vibrational-Raman scattering:

$$\left(\frac{d\sigma}{d\Omega}\right)^{\text{vib}} = \frac{\pi^2}{\epsilon_0^2}(\tilde{\nu}_0 \mp \omega)^4 \frac{\pm b_v^2}{1 - \exp(\mp hc\omega/k_B T)} \left(a'^2 + \frac{7}{45}\gamma'^2\right) \tag{21}$$

The differential cross section of individual rotational-vibrational-Raman lines is calculated by

$$\left(\frac{d\sigma}{d\Omega}\right)_{v,J}^{\text{vib-rot}} = \frac{\pi^2}{\epsilon_0^2}(\tilde{\nu}_0 \mp \Delta\tilde{\nu})^4 \frac{\exp\left(-\frac{hcB_v J(J+1)}{k_B T}\right)}{k_B T/2hcB_0} \cdot g_N \Phi_J \,, \tag{22}$$

where g_N accounts for the statistical weight of the nuclear-spin. The term Φ_J takes the form

$$\Phi_J = \frac{7}{30}\frac{[J \pm 1]\,([J \pm 1] + 1)}{2[J \pm 1] + 1}\gamma^2 \tag{23}$$

for pure Stokes and Anti-Stokes rotational transitions. The necessity of an intermediate state becomes apparent as the equation uses $\Delta J = \pm 1$ but ultimately transitions to $\Delta J = \pm 2$. For combined vibrational-rotational lines, the term Φ_J must also include the Boltzmann distribution for the vibrational states:

$$\Phi_J = \frac{b_v^2}{1 - \exp\left(-hc\omega/k_B T\right)}\frac{7}{30}\frac{[J \pm 1]\,([J \pm 1] + 1)}{2[J \pm 1] + 1}\gamma'^2 \tag{24}$$

for the S- and O-Branch, respectively, and

$$\Phi_J = \frac{b_v^2(2J+1)}{1 - \exp\left(-hc\omega/k_B T\right)}\left[a'^2 + \frac{7}{45}\frac{J(J+1)}{(2J-1)(2J+3)}\gamma'^2\right] \tag{25}$$

for Q-Branch transition. It is important to note that these expressions assume simple linear molecules, like Nitrogen and Oxygen.

Molecule	$\boldsymbol{a^2}$ [$\mathrm{m^6}$]	$\boldsymbol{\gamma^2}$ [$\mathrm{m^6}$]	$\boldsymbol{a'^2}$ [$\mathrm{m^4/kg}$]	$\boldsymbol{\gamma'^2}$ [$\mathrm{m^4/kg}$]
N_2	3.92×10^{-80}	0.64×10^{-80}	3.24×10^{-34}	5.24×10^{-34}
O_2	3.29×10^{-80}	1.56×10^{-80}	4.89×10^{-34}	8.00×10^{-34}

Table 3: Polarizability constants for N_2 and O_2 from U. Wandinger, 2005b.

The polarizability constants in Table 3 were used to calculate the backscattering cross sections for Rayleigh, Stokes vibrational, single-line Stokes rotational and and single-line S-branch scattering, as shown in Table 4.

The Rayleigh cross section is about two orders of magnitude stronger than

Molecule	$\left(\frac{d\sigma}{d\Omega}\right)^{\text{Ray}}$	$\left(\frac{d\sigma}{d\Omega}\right)^{\text{vib}}$	$\left(\frac{d\sigma}{d\Omega}\right)^{\text{vib-rot}}_{v=0}$	$\left(\frac{d\sigma}{d\Omega}\right)^{\text{vib-rot}}_{v=1}$
$\mathbf{N_2}$	6.21×10^{-32}	3.54×10^{-35}	5.32×10^{-34}	3.02×10^{-82}
$\mathbf{O_2}$	5.27×10^{-32}	3.95×10^{-35}	1.60×10^{-34}	1.03×10^{-82}

Table 4: Scattering cross sections for N_2 and O_2 at T=300K and incident wavelength 532nm in m^2/sr. J=10 and $g_N = 6$ is used for N_2 and J=13 and $g_N = 1$ for O_2. Calculated by the author.

single rotational lines (U. Wandinger, 2005a), which is also depicted in Figure 3. The Stokes vibrational cross section including all possible rotational transitions is even smaller than that, while the individual Stokes vibrational-rotational lines are multiple orders of magnitude smaller. With the high frequency shift due to the vibrational transition, a simulataneous change of the rotational state, will still be detectable at roughly the same wavelength, making it viable to use a Stokes vibrational-Raman channel. As single lines of pure rotational transitions produce a distinct enough frequency shift, a pure rotational-Raman channel might detect individual or multiple closely spaced lines.

3.3 Atmospheric Parameters

The Lidar equation (2) shows a dependency of the backscattered signal on the athmospheric parameters: extinction α and backscatter β, which can be split into their molecular and particle contributions.

The molecular extinction profile is given by (U. Wandinger, 2005a):

$$\alpha^{\text{mol}}(z) = \sigma^{\text{mol}} N(z)\,, \tag{26}$$

where σ^{mol} can be approximated by the Rayleigh cross section from Equation 16. $N(z)$ represents the molecular number density of atmospheric particles. Using the ideal gas law, we can write N as $\frac{p}{RT}$. Thus,

$$N(z) = N_s \frac{p(z) T_s}{T(z) p_s}\,, \tag{27}$$

where N_s=$2.547 \times 10^{25}\,\text{m}^{-3}$ is the molecular number concentration for standart conditions T_s=288 K and p_s=1013.25 hPa (Behrendt, 2005). This provides an expression for the molecular extinction profile, requiering only the pressure and temperature profiles and the wavelength of the light.

The extinction-to-backscatter ratio - called Lidar ratio - for elastic scattering

at molecules is approximated by (Baars, A. Ansmann, et al., 2012):

$$L_{\lambda_0}^{\mathrm{mol}}(z) = \frac{\alpha_{\lambda_0}^{\mathrm{mol}}(z)}{\beta_{\lambda_0}^{\mathrm{mol}}(z)} = \frac{8\pi}{3}\,\mathrm{sr}\,. \tag{28}$$

For inelastic processes, however, the molecular backscatter coefficient is calculated by (A. Ansmann and Müller, 2005)

$$\beta_{\lambda_{Ra}}^{\mathrm{mol}} = \left(\frac{d\sigma}{d\Omega}\right) N(z)\,, \tag{29}$$

using the differential cross sections from the previous section.

To determine the particle coefficients, either the Klett method or the Raman method can be used (Baars, A. Ansmann, et al., 2012).

The **Klett method** exploits the fact that the lidar ratio for particles, $L_{\mathrm{par}}(z)$, is constant for different types of aerosols. If the type of aerosol is known, $\alpha_{\mathrm{par}}(z)$ can be replaced by $L_{\mathrm{par}}(z) \cdot \beta_{\mathrm{par}}(z)$. Consequently, the Lidar equation becomes dependent only on $\beta_{\mathrm{par}}(z)$, which can then be determined by fitting it to the backscattered signal.

The **Raman method** uses separate measurements of the elastic and Raman signal. For the total elastic signal, Equation 2 becomes

$$P_{\lambda_0}(z) = P_0 \frac{O(z)}{z^2} C_s(\lambda_0)\beta_{\lambda_0}(z)T_{\lambda_0}^2(z) \tag{30}$$

and for the Raman signal

$$P_{\lambda_{Ra}}(z) = P_0 \frac{O(z)}{z^2} C_s(\lambda_{Ra})\beta_{\lambda_{Ra}}(z)T_{\lambda_0}(z)T_{\lambda_{Ra}}(z)\,. \tag{31}$$

A key difference from the elastic signal is the transmittance term, which is based on the Raman-wavelength on the way back to the Lidar. In addition, while elastic scattering occurs on both molecular (Rayleigh) and particulate (Mie) matter, the Raman scattering detected by the system only occurs on molecules. Therefore, $\beta_{\lambda_{Ra}}$ is equivalent to Equation 29 (A. Ansmann and Müller, 2005).

By taking the logarithm of Equation 31 and differentiating, we can rearange to get

$$\alpha_{\lambda_0} + \alpha_{\lambda_{Ra}} = \frac{d}{dz} \ln\left(\frac{N(z)O(z)}{P_{\lambda_{Ra}}(z)z^2}\right) \tag{32}$$

The molecular part of the extinction coefficients can be moved to the right-hand side of the equation. The Angstrom exponent å describes the wavelength depen-

dency of the particle extinction coefficient:

$$\frac{\alpha_{\lambda_0}^{\text{par}}(z)}{\alpha_{\lambda_{Ra}}^{\text{par}}(z)} = \left(\frac{\lambda_{Ra}}{\lambda_0}\right)^{\text{å}} \tag{33}$$

Typical values for various aerosole types are listed in Table 5. The Raman method

Aerosol	**å (0.35–0.55 µm)**	**å (0.55–0.8 µm)**
Cont. clean	1.10	1.42
Cont. average	1.11	1.42
Cont. polluted	1.13	1.45
Urban	1.14	0.43
Marit. clean	0.12	0.08
Marit. polluted	0.41	0.35
Marit. tropical	0.07	0.04

Table 5: Angstrom exponent for various aerosol types, for wavelengths of 350-550 nm and 550-800 nm from A. Ansmann and Müller, 2005.

yields the atmospheric particle extinction coefficient profile:

$$\alpha_{\lambda_0}^{\text{par}}(z) = \frac{\frac{d}{dz}\ln\left(\frac{N(z)O(z)}{P_{\lambda_{Ra}}(z)z^2}\right) - \alpha_{\lambda_0}^{\text{mol}}(z) - \alpha_{\lambda_{Ra}}^{\text{mol}}(z)}{1 + \left(\frac{\lambda_0}{\lambda_{Ra}}\right)^{\text{å}}} \tag{34}$$

The determination of the particle backscatter coefficient profile, is acquired by taking the ratio of $P_0(z)$ and $P_0(z_0)$ at reference height z_0, which eliminats the system constant, to rearange to

$$\beta_{\lambda_0}(z) = \beta_{\lambda_0}(z_0)\frac{P_{\lambda_0}(z)}{P_{\lambda_0}(z_0)}\frac{z^2 O(z_0)}{z_0^2 O(z)}\frac{T_{\lambda_0}^2(z_0)}{T_{\lambda_0}^2(z)}\,. \tag{35}$$

Including the ratio of the Raman counterpart, additionally removes the overlap function:

$$\beta_{\lambda_0}(z) = \beta_{\lambda_0}(z_0)\frac{P_{\lambda_0}(z)}{P_{\lambda_0}(z_0)}\frac{P_{\lambda_{Ra}}(z_0)}{P_{\lambda_{Ra}}(z)}\frac{N(z)}{N(z_0)}\frac{T_{\lambda_0}(z_0)T_{\lambda_{Ra}}(z)}{T_{\lambda_0}(z)T_{\lambda_{Ra}}(z_0)}\,. \tag{36}$$

The particle backscatter coefficient at the reference height z_0 must be estimated a priori (Baars, A. Ansmann, et al., 2012).

The ability to calculate these atmospheric parameters are a crucial part for determining the cross-talk effect.

4 Optical Filters and Cross-talk Effect

Multichannel systems require the ability to separate incoming light into its constituent parts. Therefore, different optical components are employed. This chapter focuses on interference filters, beam splitters, and neutral density filters, all of which are integral components of optical filters used in various Lidar systems. Additionally, we will discuss the inaccuracies in spectral separation, known as the cross-talk effect. The works of Bass, 2010 and Hecht, 2017 will be used extensively to explain the filter techniques, so further citing is refrained.

4.1 Beam Splitter

The purpose of a beam splitter is to divide an incident beam into two beams, propagating in different directions. The simplest realization is through plane-parallel plates, typically oriented at 45° to the incident beam, resulting in one beam being reflected at 90° and another transmitted at 0°. The plates have dielectric coatings, typically constructed from thin layers of magnesium or fluoride. The transmitted beam experiences a lateral displacement due to the increased refractive index within the medium. A beam-splitting cube, consisting of two optical prisms glued together with resins—a highly viscous material—circumvents these displacements but exhibits slight absorption.

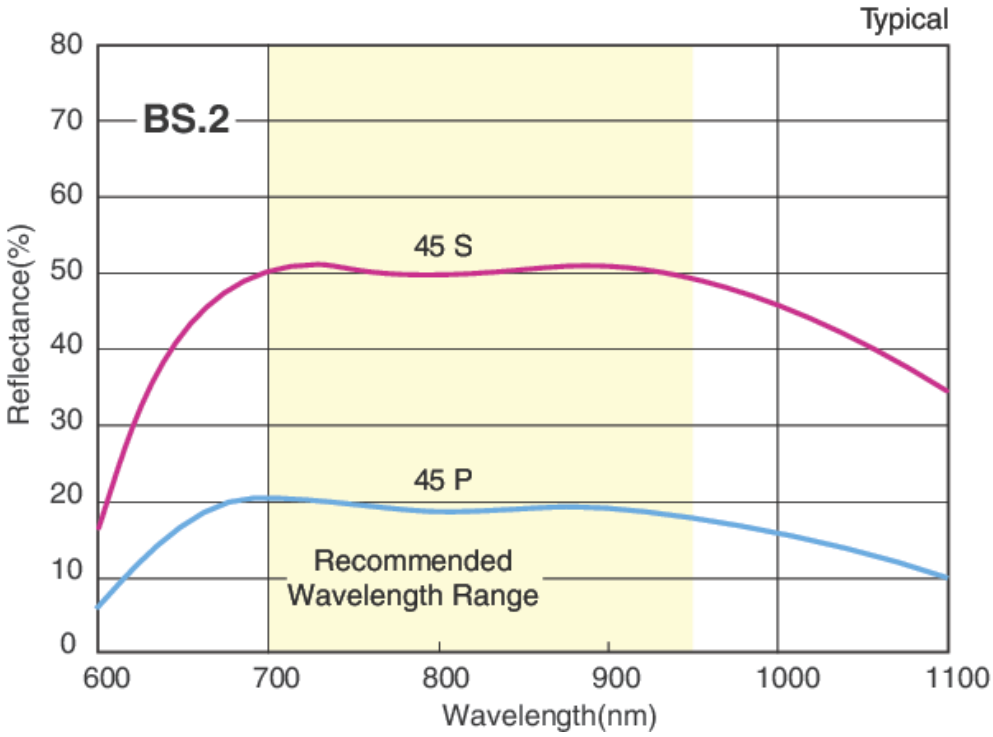

Figure 4: Reflectance of a dielectric-coated beam-splitting plate oriented at 45° with the wavelength range 700-950 nm, for S and P polarization (Newport Corporation, 2024).

There are three categories of beam splitters. The first type, called an achromatic or neutral beam splitter, divides a non-polarized beam into two beams that are identical in their spectrum. The reflectance R and transmittance T change with polarization, but remain constant across the spectrum, which is demonstrated in Figure 4. In Lidar systems, this beam splitter comes into play for analyzing light based on its polarization.

Non-polarizing beam splitters can separate the beam independent of wavelength and polarization. It is constructed by a single layer on the face of a high-refractive index prism (Azzam, 1985). Unfortunately, there is a high dependence on the angle of incidence, as Figure 5 shows.

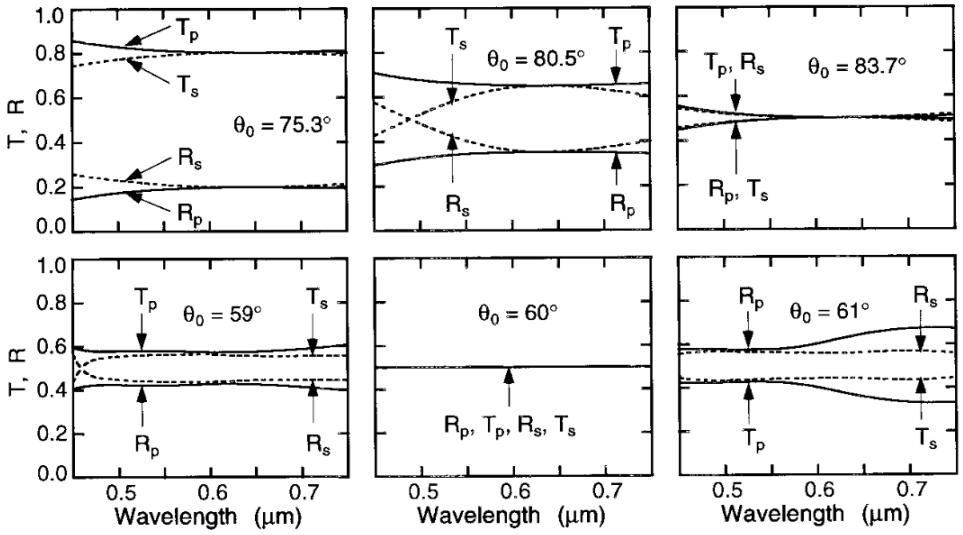

Figure 5: Transmittance and Reflectance of a single layer (n=1.533) on a prism (n_s=2.35) (Azzam, 1985) (top), and 15-layer beam splitter (Macleod and Milanovic, 1992) (bottom), near their respective design angles.

Color-selective beam splitters, or dichroic mirrors, are cut-off filters that ideally transmit light below a cut-off wavelength and reflect everything above it, or vice versa. Cut-off filters are constructed from periodic multilayers, typically composed of two layers A and B with refractive indices n_A and n_B and thicknesses d_A and d_B. By doing a N-fold repetition of the multilayer, denoted by $[AB]^N$, the first-order high reflectance zone occurs at

$$n_A d_A + n_B d_B = \frac{\lambda_1}{2} \tag{37}$$

and subsequent zones at

$$N(n_A d_A + n_B d_B) = q\frac{\lambda_q}{2}, \quad q = 2, 3, 4, \ldots \tag{38}$$

The combined spectrum, as illustrated in Figure 6, creates a highly reflective

band between two cut-off wavelengths. One can construct a $[(0.5A)B(0.5A)]^N$ multilayer, where (0.5A) denotes the layer A with half its thickness. For $n_A > n_B$ this multilayer has a higher transmittance in the longer wavelength section, effectively creating a low pass filter. Otherwise, if $n_A < n_B$, shorter wavelengths have an increased transmittance, creating a high pass filter.

The relative width of the high-reflactance zone is given by

$$\frac{\Delta\lambda}{\lambda} = \frac{4}{\pi} \arcsin\left(\frac{n_B - n_A}{n_B + n_A}\right). \tag{39}$$

The closer the refractive indexes n_A and n_B are, the narrower the width of the reflactance zone and the more layers requiered to achieve a high reflectance. The maximum reflectance is calculated with

$$R_{\max} = \left[\frac{n_m/n_s - (n_A/n_B)^{2N}}{n_m/n_s + (n_A/n_B)^{2N}}\right]^2, \tag{40}$$

where n_m and n_s describe the refractive indexes of the surrounded medium -which is air in most cases- and of the substrate the multilayer is deposited on. As the number of layers increase a higher reflectance can be achieved. The transmittance throughout the rejection region can typically be reduced below 0.1%.

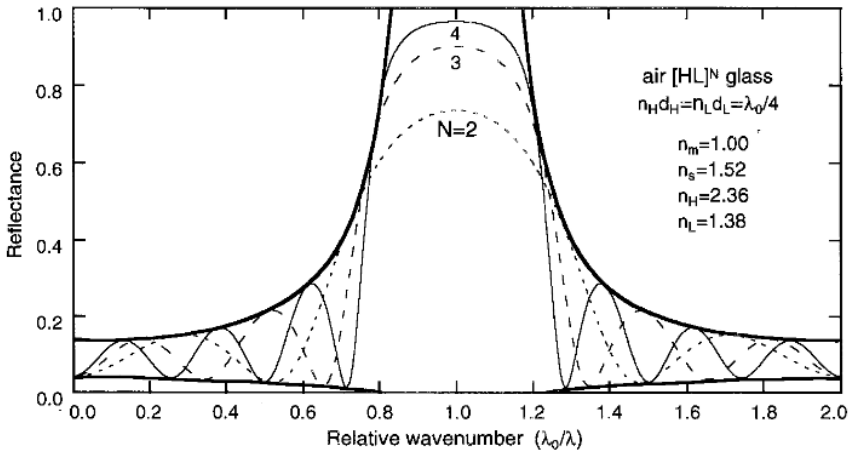

Figure 6: Calculated reflectance of a periodic multilayer of type $[AB]^N$, by Bass, 2010.

4.2 Interference Filters and Neutral Density Filters

A common type of interference filter is the Fabry-Perot filter, which consists of two reflective plates separated by a distance t, enclosing an etalon. Due to destructive interference at wavelengths other than $2t/N$, this optical instrument effectively transmits narrow-band signals. High reflectivity is achieved by sym-

metric multilayers such as $[ABAB\ BABA]$, where $n_A > n_B$. The transmission is calculated via

$$T(\lambda) = \frac{1}{1 + F \sin^2(2\pi t/\lambda)}, \tag{41}$$

with the coefficient of finesse F, which impacts the shape of the intensity pattern with the full width at half maximum (FWHM) of $\frac{4}{\sqrt{F}}$. Similar to the multilayer system for beam splitters, the maximum transmission is influenced by n_m and n_s, with

$$T_{\max} = 1 - \left(\frac{n_m - n_s}{n_m + n_s}\right)^2 . \tag{42}$$

The respective transmission and reflection curves of multilayers shift to shorter wavelenghts as the angle of incidence θ increases. The central wavelength of a Fabri-Perot filter follows the dependy (Koonen, 2006)

$$\lambda \propto \frac{1}{cos(\theta)} . \tag{43}$$

PMTs used for signal detection are susceptible to high-intensity light. Therefore, the separated signal may pass through gray filters, also known as neutral density filters. These optical instruments attenuate the signal uniformly throughout the spectrum. Typical materials include absorbing glass and evaporated films of metals like aluminium or chromium.

The optical density of a gray filter is described by the formula

$$d = -log_{10}\frac{I}{I_0} \tag{44}$$

with the intensity of incident light I_0 and the intensity after passing threw the filter I. The optical density rises linearly with the thickness of the filter. Gray filters have a high absorbing cross-section, affecting light of a broad wavelength range equally.

4.3 Cross-talk Effect

The ability of the discussed optical instruments to separate signals with different frequencies is inherently limited. Neither dichroic mirrors nor interference filters achieve a transmittance or reflectance of 100% in practice. Therefore, a fraction of light from various signals enter channels specified for different signals. This spectral leakage, also known as cross-talk, affects the detected signal strength in each channel.

In Lidar terms, the real incoming signal entering the receiver is labeled as the attenuated backscatter β^{att}. The fraction of the attenuated backscatter that

actually gets measured at a channel depends on the wavelength dependent transmission curves $T(\lambda)$ of that channel, which arise from the color-selective beam splitters and interference filters, as well as the system efficiency K, resulting from uniform optical attenuation and the photoelectric response of the detectors. Taking the spectral integral of their products yields the measured signal of channel x:

$$P_{\lambda_x}^{\text{meas}} = K_x \cdot \int_0^\infty T_x(\lambda)\beta^{\text{att}}(\lambda)d\lambda \tag{45}$$

In practice the system handles with individual backscattered signals at central wavelengths λ_N, turning Equation 45 into a sum. As $\beta^{\text{att}}(\lambda_N)$ is initially not available, the Lidar equation is used to obtain the relation

$$\beta^{\text{att}}(\lambda_N) = \frac{P_{\lambda_N}}{C_s(\lambda_N)}\,, \tag{46}$$

while C_s encapsulates the system efficiency and the filters transmission for the channels central wavelength:

$$C_s(\lambda_N) = K_N \cdot T_N(\lambda_N) \tag{47}$$

Consequently, the measured signal of channel x can be expressed as a linear combination of each cross-talk corrected signal:

$$P_{\lambda_x}^{\text{meas}} = K_x \cdot \sum_N T_x(\lambda_N)\frac{P_{\lambda_N}}{C_s(\lambda_N)} \tag{48}$$

Thus, the correction of a single channel can be calculated with

$$P_{\lambda_x} = P_{\lambda_x}^{\text{meas}} - \sum_{N\neq x} \frac{T_x(\lambda_N)}{T_x(\lambda_x)}\frac{C_s(\lambda_x)}{C_s(\lambda_N)}P_{\lambda_N}\,. \tag{49}$$

For clarity, regarding a single channel x affected by only one signal y through cross-talk, the term

$$\gamma = \frac{T_x(\lambda_y)}{T_x(\lambda_x)}\frac{C_s(\lambda_x)}{C_s(\lambda_y)} \tag{50}$$

defines the dependent/effective cross-talk, through its dependence on the system constants. Whereas the independent/real cross-talk merely relies on the transmission of the channel's filters:

$$\eta = \frac{T_x(\lambda_y)}{T_x(\lambda_x)} \tag{51}$$

5 Methodology

This chapter details the methods used to collect the necessary data and implement the discussed equations to retrieve the real and effective cross-talk values from the atmospheric properties: extinction and backscatter.

5.1 Measurement Device: Polly_1v2

The Polly_1v2 device is a Raman Lidar system developed by TROPOS. Originally, the Polly_1st device only consisted of the elastic and vibrational-Raman channels at wavelengths 532 nm (λ_0) and 607 nm (λ_{VR}), respectively. In 2016, it was upgraded to Polly_1v2, adding a rotational-Raman channel at 530 nm (λ_{RR}) for Anti-Stokes lines. Additionally, the elastic channel was split to measure co- and cross-polarized light, aiding in the analysis of depolarization effects. The provided wavelengths can be determined by the Raman shifts for Nitrogen calculated in Table 2 using Equation 7.

Polly_1v2 emits laser pulses with a height resolution of 7.5m at a repetition rate of 15Hz, allowing measurements up to an altitude of 48km. The received photons from 450 shots are summed up, resulting in a time resolution of 30s. A 5th-degree polynomial correction accounts for dead time of the PMTs, and background measurements are taken before each laser pulse. The system includes a rain detector to automatically shut down the beam and telescope during precipitation. Furthermore, the system frequently calibrates the depolarization angle, which temporarely effects the signal quality.

The optical setup for signal seperation is illustrated in Figure 7.

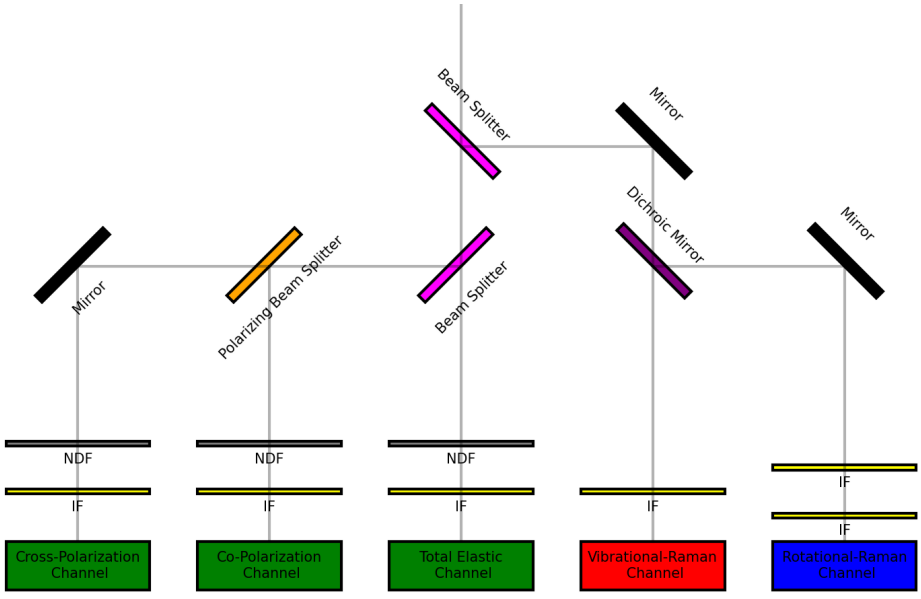

Figure 7: Optical setup of Polly_1v2.

Throughout its lifespan, Polly_1v2 has been stationed primarily at the TROPOS Science Park in Leipzig, but it has also participated in the field campaigns in Haifa (2020-2021) and Tirana (2022-2023). In this thesis data from the Tirana campaign and Leipzig data from 2018-2019, from now on referred to Leipzig campaign, is analysed.

5.2 Data Acquisition

The PollyNET website (TROPOS, 2024b) generates attenuated backscatter profile plots, displayed over periods of up to 6 hours. These plots are instrumental in identifying datasets with stable cloud layers over extended periods, which are crucial for accurate cross-talk value determination. For calculating Lidar constants, clear datasets, free of aerosols and clouds are required. All datasets used in this study were collected during nighttime to minimize the impact of daylight on the inelastic channels.

Data from all TROPOS Lidar devices are transmitted to the RSD2-server. The individual datasets, containing the signal data, measurement shots, and further relevant information, are stored as netCDF files. The number concentration of particles is derived from temperature and pressure profiles provided by the GDAS1 files, also stored on the RSD2 server. The GDAS1 data, created by the National Weather Service's National Centers for Environmental Prediction (NCEP), consists of meteorological information at specific altitudes. The resolution of these profiles typically exceeds the height resolution of the Lidar systems, requiring interpolation between the data points.

5.3 Data Processing

Data processing was performed using Jupyter Notebook and additional Python scripts. The implemented program handles reading of netCDF and GDAS1 data, creating temperature and pressure profiles, and generating uncorrected signal plots for the elastic and inelastic channels. Periods of precipitation and depolarization calibration are excluded from analysis. The process continues with selecting the specific time region, where the averaged signal profile is calculated using the background and dead time corrections.

Calculating the particle extinction coefficient (34) requires the Angstrom exponent and overlap function. Assuming an aerosol-free atmosphere below any cloud layer, $\mathring{a}$ is set to 1.2, while the Angstrom exponent within the cloud is set to 0, in accordance to Table 5.

Initially, the overlap function is assumed to be 1.

Potential negative signal values, becoming present at high altitudes where the backscattered signal attenuates to the background signal level, cannot be used in the logarithmic term of Equation 34, whereas the identity

$$\frac{d}{dz} ln\left[f(z)\right] = \frac{\frac{d}{dz} f(z)}{f(z)} \tag{52}$$

enables the handling in these cases. The derivative for a dataset with discrete values is obtained by linear regression, where the slope of 41 data points, which correspond to 150m above and below the central height z—is used for height z. Additional smoothing of the particle extinction coefficient profiles is necessary, demonstrated in Figure 8, which is achieved by calculating the intercept of the linear regression at height z. Typically, smoothing ranges of 600-750m are chosen (Baars, A. Ansmann, et al., 2012), which are used for the datasets to determine the Lidar constant ratio. The evaluation of the dependent cross-talk coefficient, however, requires precise extinction profiles near the cloud layer, thus smaller smoothing ranges of 21 data points—75m above and below height z—are used.

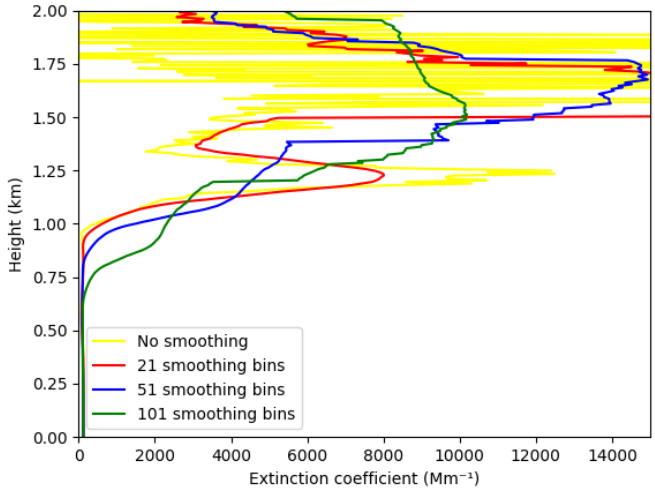

Figure 8: Extinction coefficient profiles calculated with various smoothing ranges for a cloud case. Using 21 smoothing bins, the trajectory at the bottom of the cloud is captured accurately.

For the calculation of the particle backscatter coefficient (36) $\beta_{\lambda_0}^{\text{par}}(z_0) = 5 \cdot 10^{-7}\,\text{Mm}^{-1}\text{sr}^{-1}$ at reference height of 500 m is used (Griesche et al., 2021). Reviewing the overlap function, we can either calculate it analytically (Ludwig, 2014) or we make use of the independence of the particle backscatter on the overlap function and apply the Klett method explained in the *Raman Lidar* chapter, to get the overlap corrected particle extinction coefficient. The overlap function

is then determined by (Ulla Wandinger and Albert Ansmann, 2002)

$$O(z) = \frac{P_{\lambda_R}(z)z^2}{C_s(\lambda_R)\beta_{\lambda_R}(z)T_{\lambda_0}(z)T_{\lambda_{Ra}}(z)} \,. \tag{53}$$

Figure 9 shows the overlap function of clear night datasets. Despite manual adjustments to the beam position during the campaigns, leading to frequent changes of the overlap profiles, $O(z)$ generally reaches 1 by at least 500 m. For all cloud layers observed in this study, located above 1 km, the overlap function for the extinction profile is ignored.

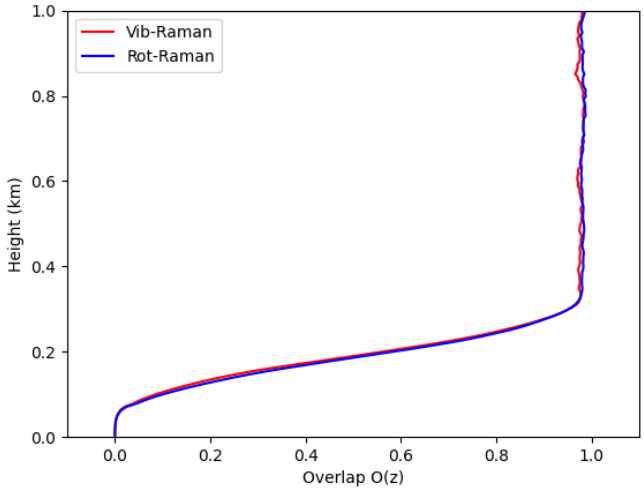

Figure 9: Overlap function of May 7, 2023 from Tirana between 01:40-02:15 UTC calculated with the vibrational and rotational Raman signal. $L_{par}(z)$ was set to 60 sr, in order to achieve a constant overlap at higher altitudes. $C_s(\lambda_{Ra})$ was choosen to normalize O(3km)=1.

5.4 Estimation of Cross-talk Parameter

The optical setup of Polly_1v2, shown in Figure 7, begins with a non-polarizing 50%/50% beam splitter. The reflected portion of it is directed to a dichroic mirror, where the vibrational-Raman signal gets seperated from the elastic and rotation-Raman signal. Each channel is equipped with an interference filter, except the rotational-Raman channel, which uses a double-stacked interference filter to filter out the elastic strong signal, as suggested by Veselovskii et al., 2015. The elastic channels are further attenuated by gray filters.

Given the significantly higher intensity of the elastic signal compared to the inelastic signals, the elastic channels are assumed to be unaffected by cross-talk. Furthermore, the dichroic mirror effectively transmits the vibrational-Raman 607 nm-signal while reflecting the 532 nm and 530 nm light, making the

vibrational-Raman channel also basically unaffected by cross-talk. However, the rotational-Raman channel is more susceptible to cross-talk. In this context, γ and η refer to the dependent and independent cross-talk values after Equations 50 and 51, corresponding to the relative spectral leakage from the total elastic signal into the rotational-Raman channel.

The cross-talk effect is more noticeable when the relative intensity of the elastic signal to the rotational-Raman signal increases. At cloud layers, the elastic signal intensifies due to particle backscattering on water molecules, while both Raman signals attenuate. Thus, cloud layers are well-suited for determining the dependent cross-talk value, which is demonstrated in Figure 10.

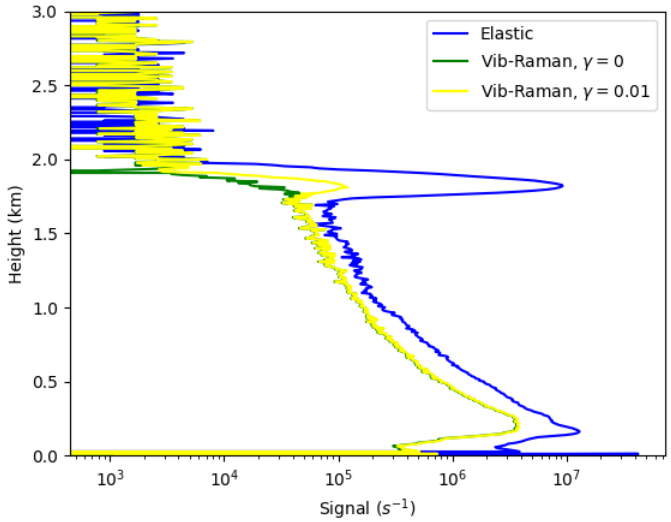

Figure 10: Measured signal strength of the elastic signal, the assumed to be unaffected vibrational-Raman signal, and the vibrational-Raman signal with a hypothetical dependent cross-talk value of 0.01.

Determining the effective cross-talk value γ can either be done by direct calculation or by approximation through error minimization.

The **direct method** utilizes the fact that, at cloud layers, the particle extinction coefficient significantly exceeds the molecular extinction and the Angstrom exponent becomes 0. This implies that the transmittance is independent of the wavelength in this region (U. Wandinger, 2005b). Taking the signal ratio of the two Raman signals, all terms cancel out except the system constants and transmittance ratio, which remain constant. This leads to a constant ratio $\frac{P_{\lambda_{RR}}}{P_{\lambda_{VR}}}$. If the cross-talk correction is not applied to the rotational-Raman signal profile, the result will deviate from this:

$$\frac{P^{\text{corr}}_{\lambda_{RR}}(z)}{P_{\lambda_{VR}}(z)} = \frac{P^{\text{meas}}_{\lambda_{RR}}(z) - \gamma P^{\text{meas}}_{\lambda_0}(z)}{P_{\lambda_{VR}}(z)} = \text{const.} \tag{54}$$

Taking the derivative with respect to z and rearranging after γ leads to

$$\gamma = \frac{P_{\lambda_{VR}}(z)' \cdot P_{\lambda_{RR}}(z) - P_{\lambda_{RR}}(z)' \cdot P_{\lambda_{VR}}(z)}{P_{\lambda_{VR}}(z)' \cdot P_{\lambda_0}(z) - P_{\lambda_0}(z)' \cdot P_{\lambda_{RR}}(z)} \,. \tag{55}$$

To evaluate the cross-talk effect through the similarity of the particle extinction coefficient profiles, the mean squared error (MSE) is used as the metric:

$$MSE(\gamma) = \int \left(\alpha^{par}_{\lambda_{VR}}(z) - \alpha^{par}_{\lambda_{RR}}(z,\gamma)\right)^2 \tag{56}$$

Minimizing this equation over all data points in the region of interest, results in the optimal cross-talk value γ_0. This is achieved by successive approximation to an uncertainty of 1%, thus terming it **approximative method**.

Furthermore, $MSE(\gamma)$ can be approximated by a quadratic equation near its global minimum:

$$MSE(\gamma) \approx MSE(\gamma_0) + A \cdot (\gamma - \gamma_0)^2 \tag{57}$$

After the transformation:

$$exp\left(1 - \frac{MSE(\gamma)}{MSE(\gamma_0)}\right) = exp\left(-\frac{A}{MSE(\gamma_0)}\,(\gamma - \gamma_0)^2\right) \tag{58}$$

the right-hand side of the equation resembles the un-normalized Gaussian function, with $\Delta\gamma$ as the standart deviation, which can be expressed as:

$$\Delta\gamma = \sqrt{\frac{MSE(\gamma_0)}{2A}}. \tag{59}$$

The same value is achieved by determining the full width of γ, where $MSE(\gamma)$ is below $2 \times MSE(\gamma_0)$ and dividing by $2\sqrt{2}$, which is similar to the relation of the standart deviation of a normal distribution to its FWHM.

Determining the independent cross-talk value requires the ratio of both system constants, referred to the Lidar constant ratio, which can be computed with

$$\frac{C_s(\lambda_0)}{C_s(\lambda_{RR})} = \frac{\beta_{\lambda_{RR}}}{\beta_{\lambda_0}} \cdot \frac{P_{\lambda_0}}{P_{\lambda_{RR}}} \cdot \frac{T_{\lambda_{RR}}}{T_{\lambda_0}} \,. \tag{60}$$

A clear dataset offers minimal variation in the individual profiles, resulting in a precise mean value of the Lidar constant ratio. Finally, the independent cross-talk is calculated by

$$\eta = \frac{C_s(\lambda_0)}{C_s(\lambda_{RR})} \cdot \gamma \,. \tag{61}$$

6 Results

This section presents an overview of the results obtained in this thesis. Starting of by demonstrating the determination of the dependent cross-talk, a critical aspect of this study, using both the approximative and direct methods, the chapter follows up by providing a brief demonstration of the calculation of the Lidar constant ratio. It concludes with long-term analysis diagrams from the Tirana and Leipzig campaigns, which highlight the temporal behavior of these quantities, including the independent cross-talk.

6.1 Dependent Cross-talk Determination

The accuracy of determining the dependent cross-talk value is highly influenced by the quality of the data, particularly the shape and height of the cloud layers and other environmental factors. Therefore, a case study approach is used to provide examples of both optimal and suboptimal cases.

Best cases - Comparing methods

Figure 11 shows the uncorrected signal data of the total elastic and both inelastic channels on the April 18, 2023, in Tirana, between 00:00 and 06:00 UTC, ranging up to 9 km. The subplots use a uniform logarithmic colorbar, demonstrating the expected decline in backscattered signal with increasing altitude. Between 2 and 3 km, the total elastic signal, exhibits significant increases, indicating the presence of a cloud layer. In the same regions, the rotational- and vibrational-Raman signals show strong attenuation. Notably, from 04:00 UTC onwards, the inelastic signals become saturated due to daylight background radiation, while the elastic signal remains unaffected. This highlights the necessity of neutral density filters to manage the high intensity in the elastic channels.

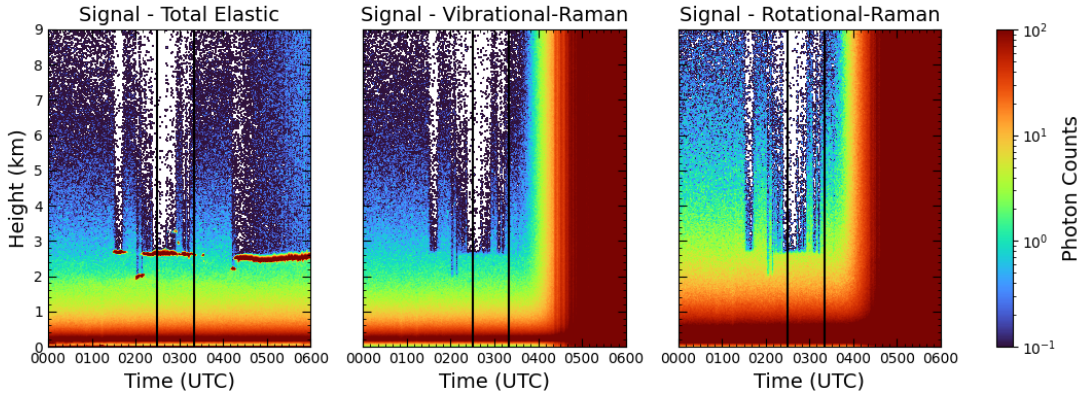

Figure 11: Raw signal from April 18, 2023, in Tirana. The time period used for further analysis is marked by the vertical black lines.

The selected time period for analysis (02:30-03:20 UTC) was used to calculate the respective particle extinction coefficient profiles, shown in Figure 12. The profile for the rotational-Raman signal (blue) appears slightly shifted to a higher altitude compared to its vibrational-Raman counterpart (red). Although the base of the observed cloud layer suggests a sharp increase in the extinction coefficient profiles, the differentiation and smoothing processes applied to the data result in smoother curves. The black lines indicate the height range (2.4–2.6 km) used to optimize the cross-talk parameter via the approximative method. The resulting cross-talk corrected rotational-Raman profile (green) aligns well with the vibrational-Raman profile from the base of the cloud layer to its peak, though it underestimates the extinction above 2.7 km.

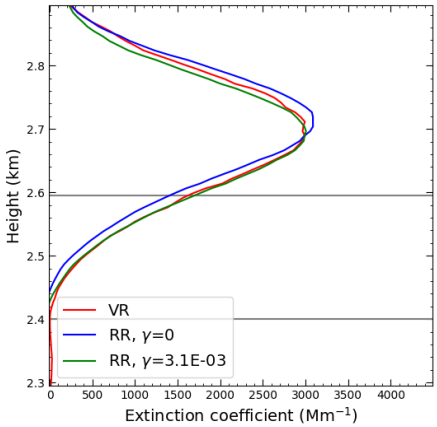

Figure 12: Particle extinction coefficient profiles at the cloud base height using the vibrational-Raman, and the uncorrected and cross-talk corrected rotational-Raman signals. The horizontal black lines indicate the height at which the cross-talk parameter was calculated.

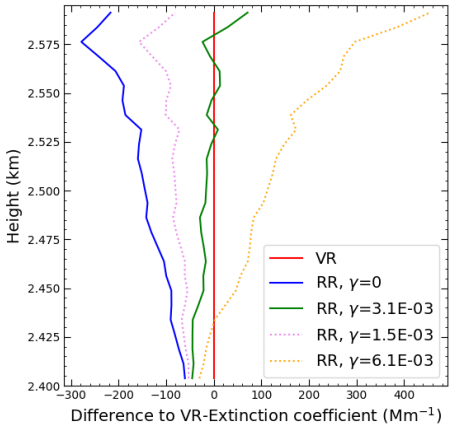

Figure 13: Comparison of the particle extinction coefficient profiles using the rotational-Raman signal with various cross-talk values.

For a more detailed comparison, Figure 13 visualizes the difference between the extinction profiles in the selected height region. The orange and purple dotted lines represent profiles using double and half of the optimal effective cross-talk value, respectively. The uncorrected and corrected profiles slightly underestimate the target profile in the first 25 meters, but only the green profile accurately captures the subsequent trend.

Figure 14 summarizes the process of searching for the optimal effective cross-talk parameter that minimizes the mean squared error of the cross-talk corrected profile compared to the reference profile, via successive approximation. The blue

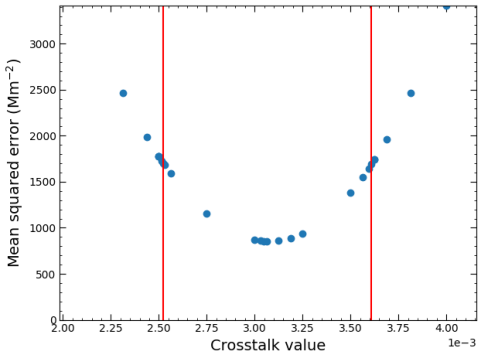

Figure 14: Error function for different cross-talk values. The minimum describes the optimal crosstalk parameter. The vertical red lines mark the region where the error exceeds twice the minimum.

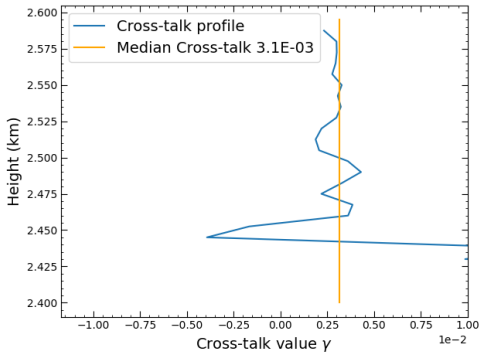

Figure 15: Dependent cross-talk profile and median value using the direct calculation method.

dots represent the tested cross-talk values and their respective errors, suggesting a quadratic progression. The region between the red lines marks where the mean error is less than twice the minimum error. The program determined an effective cross-talk value of $\gamma = 0.0031 \pm 0.0004$.

The direct calculation method, using the uncorrected signal from the same time and height section, yields individual cross-talk values for each height bin, as shown in Figure 15. The values below 2.45 km, corresponding to the start of the cloud region, are unreliable. Within the cloud layer the values remain fairly constant, and result in an overall median cross-talk value of 0.0031, showing good agreement with the aproximative method.

In a different case from February 20, 2019, in Leipzig, a constant cloud layer is observed between 1–2 km in the uncorrected signal data, shown in Figure 16). The selected time period is between 03:35 and 04:45 UTC. The uncorrected particle extinction coefficient profiles exhibit a similar behavior, appearing slightly shifted. The approximative method, calculated from 1.6–1.7 km, yields an optimal dependent cross-talk value of $3.4 \cdot 10^{-4}$ with a standard deviation of $8 \cdot 10^{-5}$, an order of magnitude smaller than the previous case. However, the cross-talk corrected extinction profile again shows good agreement with the vibrational-Raman reference profile up to 1.7 km. The direct calculation on the other hand gives a median value of $-4 \cdot 10^{-6}$ for the height range 1.65-1.75 km, highlighting the limited reliability of this method. This issue primarily stems from the height range used for taking the derivative of the signals, which can include values below the cloud layer where the method's assumptions do not hold. Therefore, only the approximative method was used for further analysis.

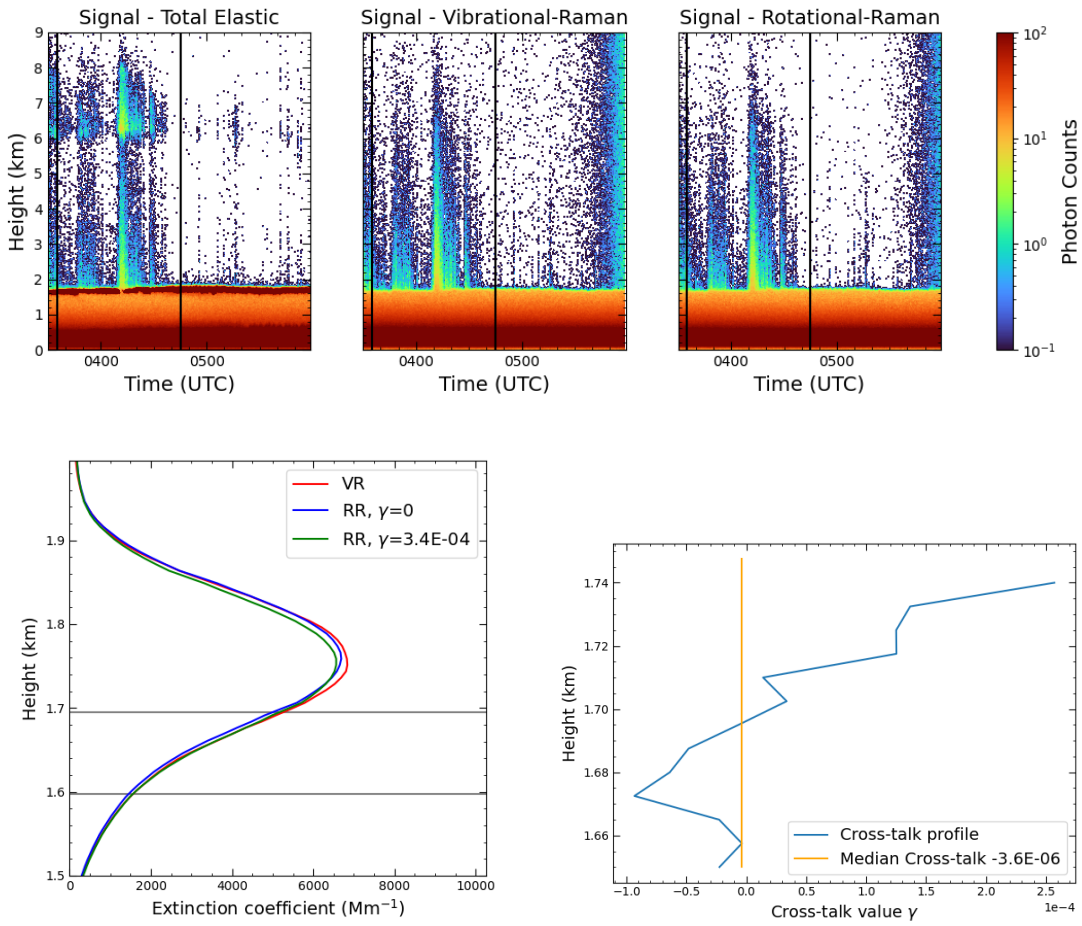

Figure 16: Case from February 20, 2019, Leipzig.

Suboptimal cases

In this study, three types of cases were identified where undesired behavior occured, complicating cross-talk determination. The first case, shown in Figure 17, presents data from June 17, 2023, in Tirana. In the uncorrected signal data, the cloud lies within a time period affected by daylight background radiation. As the inelastic signals weaken to the level of the background radiation, the background correction becomes insufficient, resulting in unpredictable extinction profiles. Consequently, cross-talk determination can only be reliably performed up to an altitude of 1.95 km in this case, yielding a dependent cross-talk parameter of 0.0018 ± 0.0006. Most datasets affected by daylight radiation are unreliable and must be excluded from the analysis.

The second type of suboptimal case occurs when there is very low signal data above the cloud layer, as demonstrated in Figure 18. The background correction in such cases results in non-positive signal values, leading to breaks in the extinction profile. Despite these challenges, cross-talk determination is still possible up to a certain altitude. By simply including data from approximately 5 minutes be-

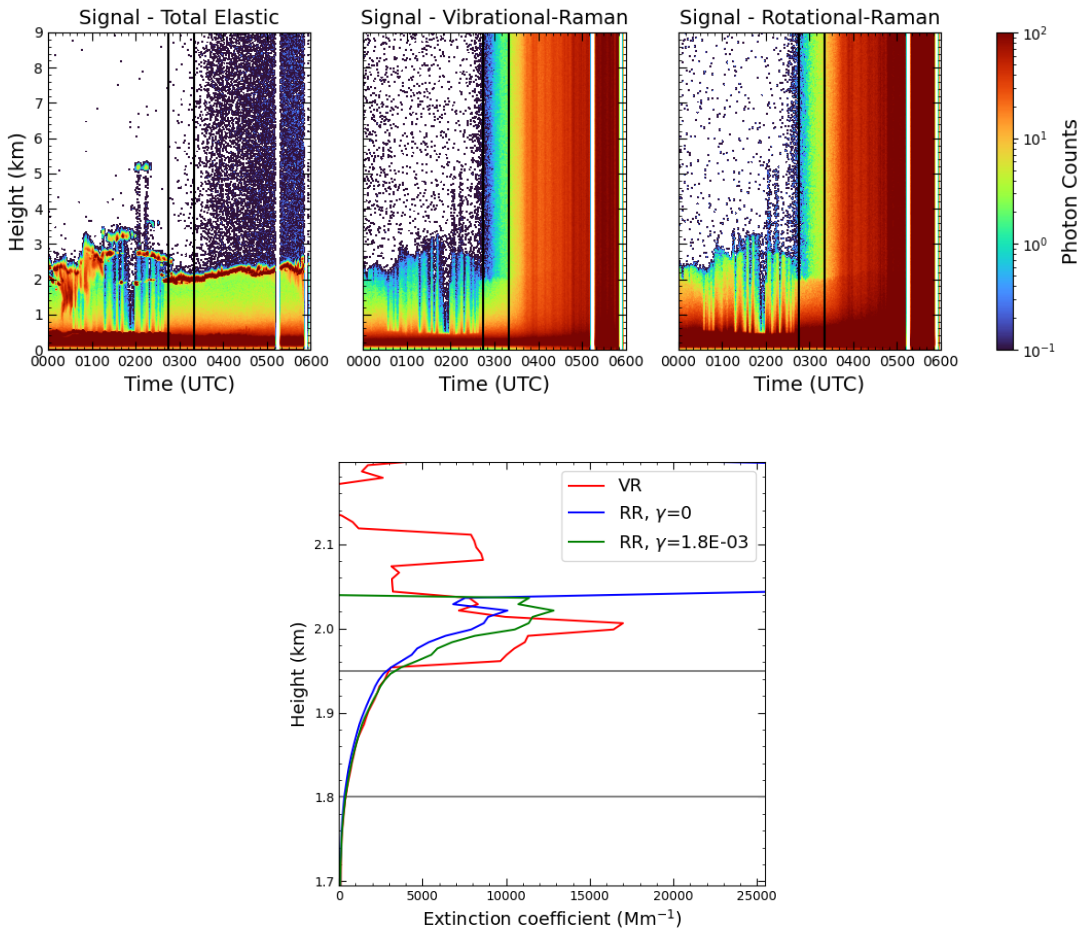

Figure 17: Case from June 17, 2023, Tirana. The background radiation begins to influence the signal at around 02:30 UTC.

fore the cloud's arrival helps provide sufficient signal strength above the cloud for smoother extinction curves. While the optimal cross-talk parameter only changes slightly, the evaluated error significantly decreases, suggesting that extending the observed time period is beneficial for datasets affected by this issue.

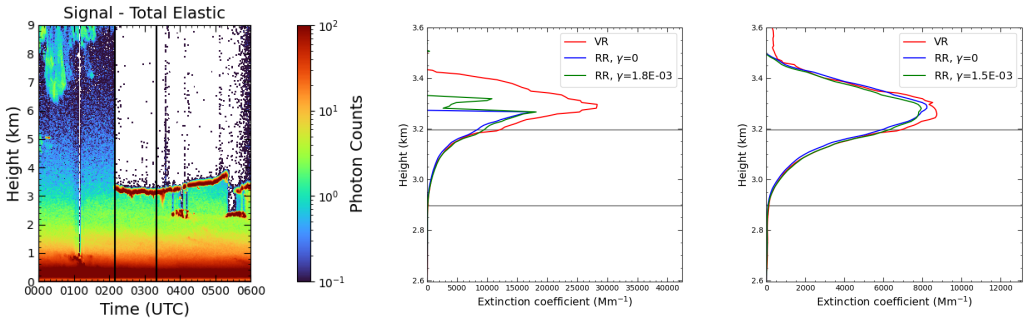

Figure 18: Case from November 16, 2023, Tirana. The first extinction profile is calculated for the time range 02:10–03:20 UTC, as shown in the signal data. The second profile results from including 10 additional time bins, corresponding to 02:05–03:20 UTC.

The third type of suboptimal case, typically occurs at high altitudes or in situations where there are attenuating layers between the ground and the investigated cloud. In such cases, much less signal data reaches the receiver, resulting in larger discrepancies between the extinction profiles. An examined cloud layer from May 12, 2018 (Leipzig) was located at 6 km height, with additional clouds between 4-5 km. This case yields a cross-talk value of 0.0004, but with an uncertainty of 0.0006, which is a significantly larger relative error than the previous cases.

This concludes the exploration and determination of the dependent cross-talk for various datasets. In the subsequent section on long-term analysis, we will evaluate the temporal behavior of the dependent cross-talk values across the entire duration of the Tirana and Leipzig campaigns.

6.2 Lidar Constant Ratio Determination

The Lidar constants provide crucial information about the performance of the Lidar system, capturing the transmission of the emitter and receiver as well as the detection coefficient. The calculation, based on Equation 60, is straightforward. Figure 19 demonstrates the determination of the Lidar constant ratio on April 18, 2023, which is the same dataset used in the first dependent cross-talk example, as it contains a clear sky from 00:00 to 01:00 UTC.

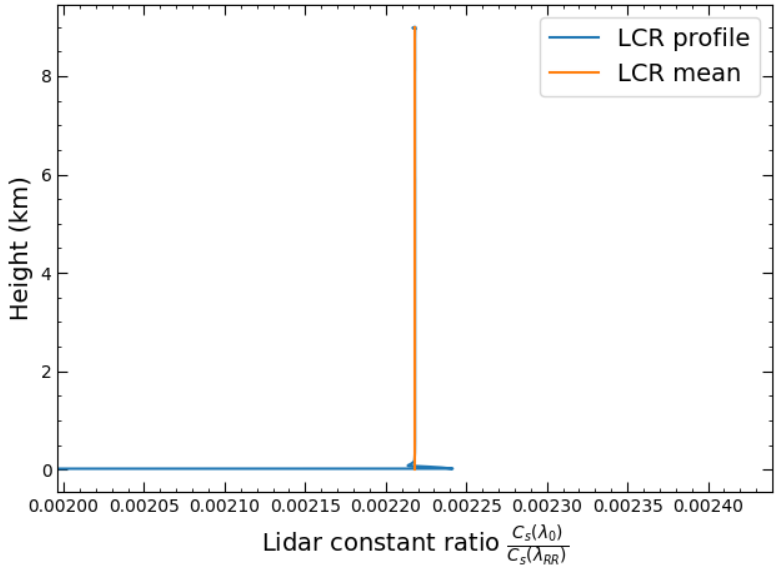

Figure 19: Lidar constant ratio on April 18, 2023, Tirana.

Neglecting the values within the first 100 m range–where the overlap is 0, the profile stays constant with a mean value of 0.0022. Multiplying this ratio by the respective effective cross-talk yields the real cross-talk value $\eta = 6.8 \times 10^{-6}$.

We expect the Lidar constants to remain temporally consistent as long as the optical setup remains unchanged. However, Figure 20 shows significant variations in the calculated Lidar constant ratio over time. During April 30 and May 6 2023, an increase occurred from 0.0038 to 0.0146, followed by relative stability until May 17 (0.0144). On June 1, the ratio decreased significantly again to 0.0051, despite no changes to the gray filters. The Polly_1v2 logbook reveals that a telescope cleaning was performed on May 3 and an overlap-correction on May 18, aligning with the abrupt changes in the Lidar constant ratio. While these procedures did not directly impact the optical setup, they provide insight into the dependencies of the method. For instance, particle accumulation on the telescope impacts signal transmission through absorption or scattering, and overlap corrections involve adjustments to the telescope's orientation, potentially affecting the angle of incidence at the optical filters, shifting the transmission profile, suggusted by Equation 43.

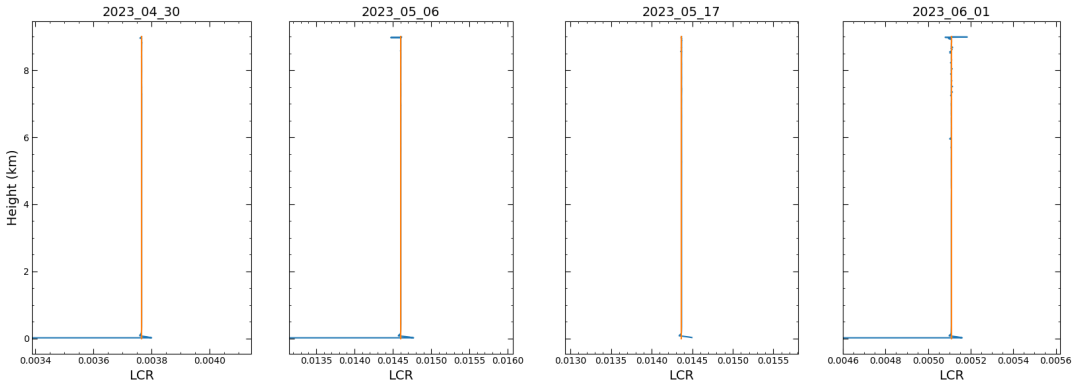

Figure 20: Lidar constant ratios on subsequent days, Tirana.

6.3 Longterm Analysis

After determining γ for every viable dataset within both campaigns and calculating the Lidar constant ratio on the same or a contemporary dataset, we obtain the longterm analysis diagrams shown in Figure 21 and 22. These diagrams illustrate the temporal behavior of these quantaties, as well as the real/independent cross-talk η. Additionally, in the second subplot, timestamps mark events of significant changes on the Lidar system. Despite the temporal variance of γ and the Lidar constant ratio, the independent cross-talk shows overall temporal consistency for the Tirana campaign, with values varying by a factor of two around the mean value of $5.5 \cdot 10^{-6}$.

The Leipzig data shows a similar pattern, but with overall less consistency and a slightly lower mean value of $\eta = 4.1 \cdot 10^{-6}$.

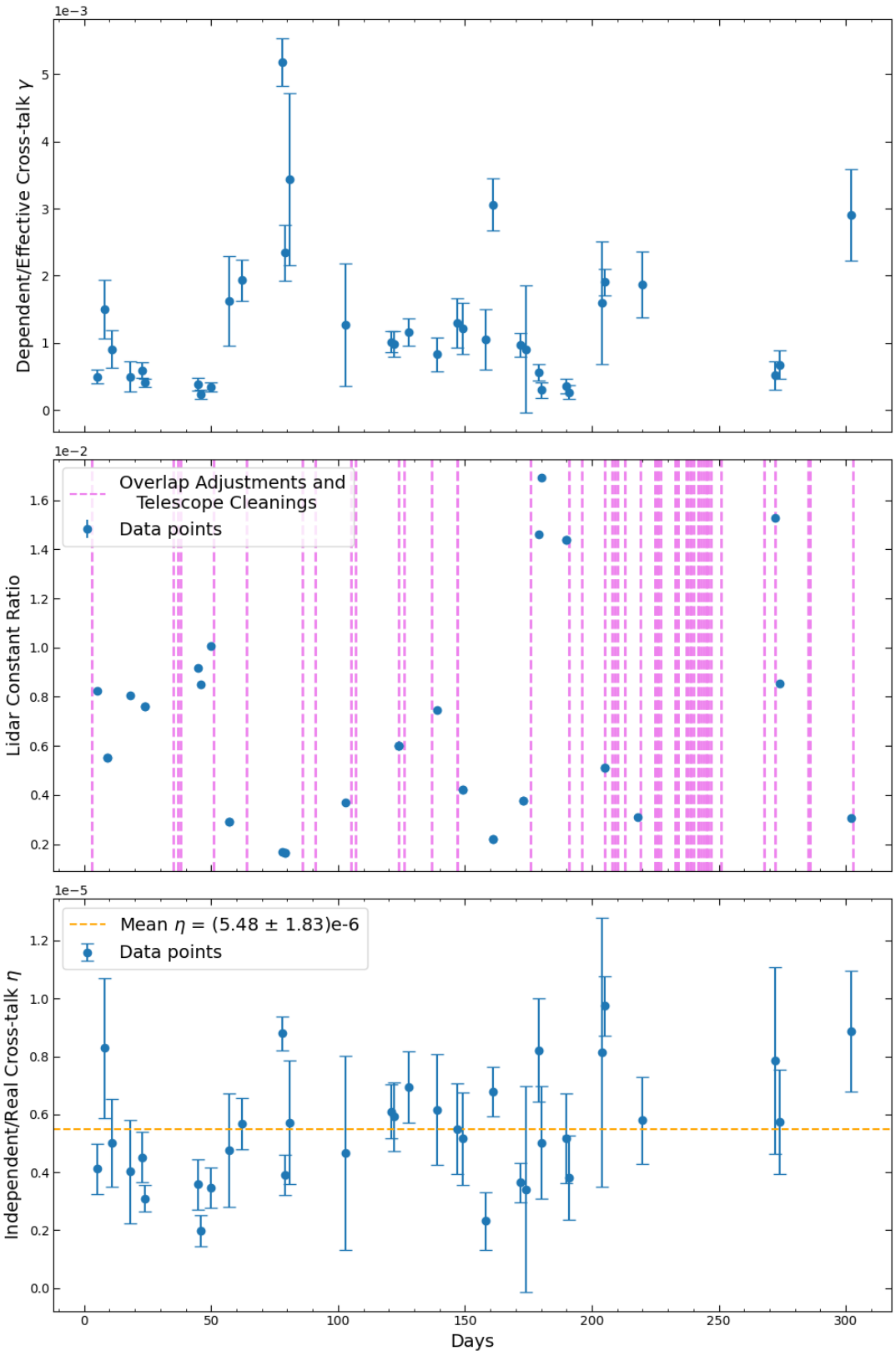

Figure 21: Evalutation of Polly_1v2 data from the Tirana campaign (November 8, 2022 - October 9, 2023).

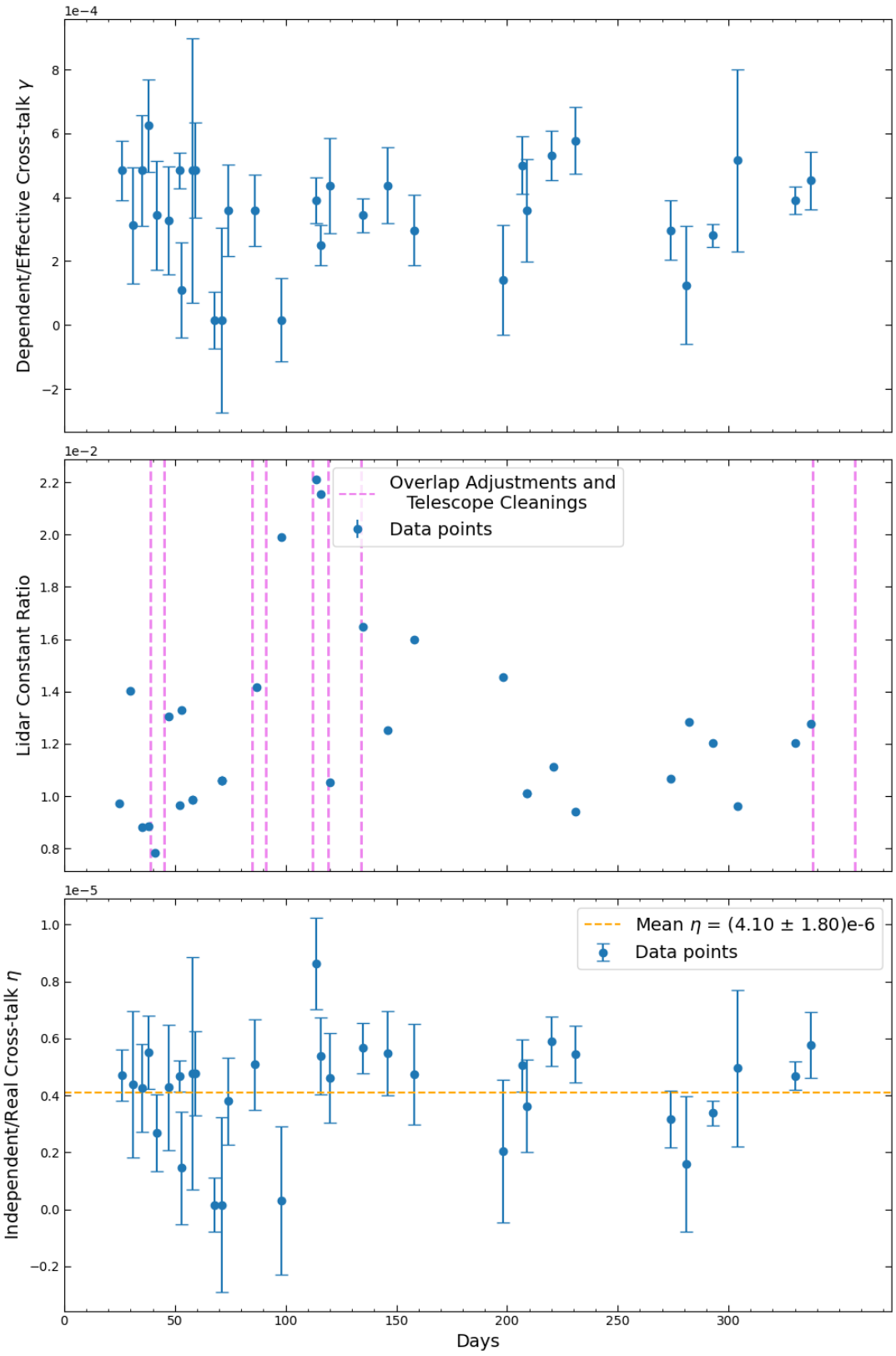

Figure 22: Evalutation of Polly_1v2 data from the Leipzig campaign (October 25, 2018 - September 13, 2019).

7 Discussion

Despite general agreement of the independent cross-talk η between both campaigns, the variation desires further explanation. This chapter provides analysis of additional potential error sources, concluding with a comparison to the actual transmission curve of the relevant interference filters.

7.1 Temperature Effects

The most significant influence on the cross-talk effect can be attributed to temperature variations. As shown in the *Raman Lidar* chapter, the differential cross sections of inelastic scattering processes, described by Equation 21 and 22, are temperature-dependent. While the measuring devices are designed to capture specific rotational-Raman lines, temperature differences at the scatterer can shift the probability distribution of these transitions, potentially moving them outside the spectral detection range. The analysis from Veselovskii et al., 2015 on a rotational-Raman Lidar shows a variance of the sum of detectable RR-cross sections of up to 3.5% in the temperature range 230-330 K.

Figure 23 attempts to determine a temperature dependency by plotting η from both campaigns against the temperature at the respective cloud base heights. However, the data does not suggest a direct dependency, possibly due to the error of the approximative method overshadowing any underlying trend.

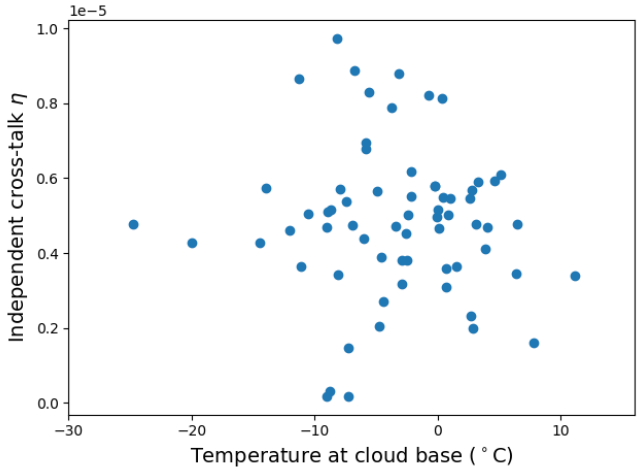

Figure 23: Temperature dependency of the independent cross-talk at the cloud base heights.

Temperature effects may also influence the divergence of the backscattered signals through the Doppler effect, and optical components might shift their transmission curves to higher wavelengths under increasing temperatures (Alluxa, 2024).

7.2 Simplifying Assumptions

Two critical assumptions were made during the application of the methods within the program, impacting the determination of γ and the Lidar constant ratio separately.

First, the Angstrom exponent å, a key parameter for the wavelength dependency of the particle extinction coefficient, was assumed to be constant at 1.2 beneath the cloud layer of interest and 0 within the cloud. This simplification disregards the variability of aerosol layers between the cloud and the Lidar system. Variations in the Angstrom exponent can induce a shift of the extinction profile significant enough to affect the determined cross-talk value γ.

Second, the assumption of a constant particle backscatter coefficient of $5 \times 10^{-7}\,\mathrm{Mm^{-1}sr^{-1}}$ at the reference height 500 m is similarly problematic. This value can vary significantly depending on time, location, and environmental factors, impacting the determination of the Lidar constant ratio. Accounting for these variations was beyond the scope of this thesis but could improve the method's accuracy.

7.3 Comparison to Transmission Curves

TROPOS has specifics of every device available on their internal Lidar-wiki. This includes the actual transmission curves of the interference filter in front of the rotational-Raman channel of the Polly_1v2. The file contains the experimental and theoretical transmission values $T_{RR}(\lambda)$ from 520-540 nm. The Nd:YAG laser has a central wavelength of 1064.6 nm with an FWHM of 1 nm (Salvadé et al., 2002). After frequency doubling, this corresponds to a central wavelength of $\lambda_0 = 532.3$ nm with a standard deviation of $\sigma = 0.2$ nm. Only regarding molecular scattering, the normalized elastic attenuated backscatter takes the Gaussian-form

$$\beta^{\mathrm{att}}_{\lambda_0}(\lambda) = \frac{1}{\sqrt{2\pi\sigma^2}} \exp\left[-\frac{1}{2}\left(\frac{\lambda-\lambda_0}{\sigma}\right)^2\right]. \tag{62}$$

The rotational-Raman counterpart encompasses the backscattering cross sections of the individual Anti-Stokes lines:

$$\beta^{\mathrm{att}}_{\lambda_{RR}}(\lambda) = \frac{\displaystyle\sum_J \frac{\left(\frac{d\sigma}{d\Omega}\right)^{\text{vib-rot}}_J}{\sqrt{2\pi\sigma^2}} \exp\left[-\frac{1}{2}\left(\frac{\lambda-\lambda_J}{\sigma}\right)^2\right]}{\displaystyle\sum_J \left(\frac{d\sigma}{d\Omega}\right)^{\text{vib-rot}}_J}, \tag{63}$$

where λ_J is calculated with Equation 7 and 15. Figure 24 depicts the overlap of these profiles. The relative transmission of the attenuated backscatter into the rotational-Raman channel, which is the definition of η (51), is then

$$\eta = \left(\frac{\int_0^\infty T_{RR}(\lambda)\beta^{\text{att}}_{\lambda_0}(\lambda)d\lambda}{\int_0^\infty T_{RR}(\lambda)\beta^{\text{att}}_{\lambda_{RR}}(\lambda)d\lambda} \right)^2 . \tag{64}$$

The square accounts for the double-stacked inteference filter, shown in Figure 7.

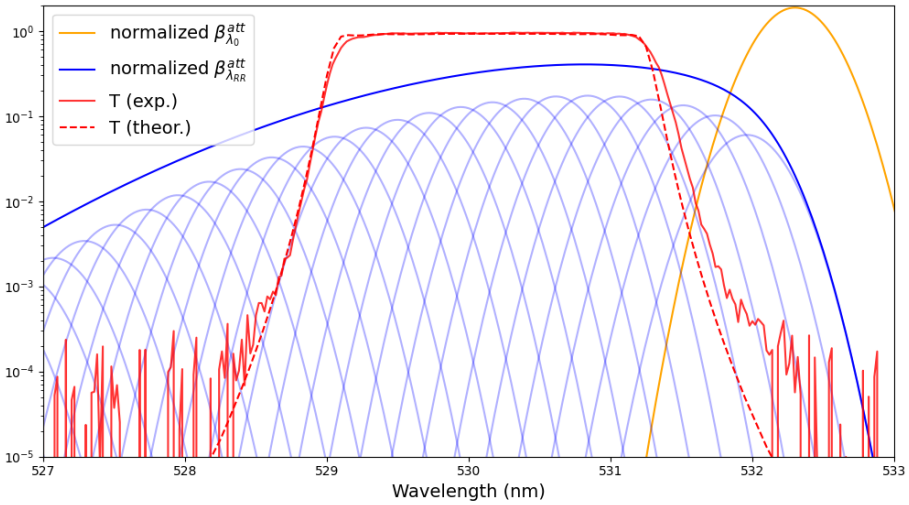

Figure 24: Spectral profile of the normalized attenuated backscatter for Rayleigh and rotational-Raman processes, with incidient wavelength 532.3 nm, and the theoretical and experimental transmission curves of the interference filter in front of the rotational-Raman channel. The light blue curves are the individual Anti-Stokes rotational-Raman lines, which add up to the dark blue profile.

The resulting independent cross-talk value is 8.4×10^{-10}, using the theoretical curve, and 6.1×10^{-8}, using the experimental curve, which are both significantly lower than the mean cross-talk parameters for the Leipzig and Tirana campaign. Potential error sources lie in disregarding the Mie contribution in Equation 62, and the oversimplification of the channel's wavelength dependent transmission on this one interference filter.

The experimental curve exhibits strong deviation next to the main transmission band, and even consists of negative values. The lokal peaks are hinting at a constant trend, which might be attributed to the relation of Equation 42. A similar behaviour between the theoretical and experimental transmission curves was observed for the rotational-Raman interference filter on the Raman Lidar PollyXT (Engelmann, Ronny et al., 2018).

8 Summary

By understanding the retrieval of different atmospheric parameters, an analytical framework could be constructed to compare the particle extinction coefficient profiles using the different inelastic signals of a Raman Lidar system. Exploring the discrepancies introduced by artificial amplification of these signals through the strong elastic scattering processes in the atmosphere, termed cross-talk, the neccessity for a correction term was concluded.

With the present optical setup in the Polly_1v2 Raman Lidar system, pre-assumptions about the significance of cross-talk effect in each channel was made, resulting in a dependent/effective cross-talk parameter, corresponding to spectral leakage of the measured total elastic signal into the rotational-Raman channel. As the most influence occurs with an increment of the relative signal's intensity, cloud cases were intensively studied. The model was extended by incorporating the ratio of the respective system constants, accounting for the channel's attenuation, to acquire the inelastic cross-talk parameter.

While the respective values of effective cross-talk and the Lidar constant ratio showed unstable behaviour, the resulting product–the real cross-talk value–comprises of an overall temporal consistency, for the Leipzig and Tirana campaign. The evaluation of such small values are prone to strong variances based on simplifiying assumptions in the methodology, as well as temperature effects, serving as an explanation for the significant deviation to the cross-talk parameter extracted from the filter's transmission curve.

Building up on this thesis work, the methods can be used for cross-talk correcting the rotational Raman channel of other devices, like the PollyXT, although, cross-talk is not exclusive for rotational-Raman channels, nor for Raman Lidar or Lidar in general. It affects every multi-channel experiment, bound by the theoretical and practical limits of spectral separation through such optical instruments. Making the effort to correct it worth it.

References

Abe, Kohji and Takeshi Shigenari (2011). "Raman spectra of proton ordered phase XI of ICE I. Translational vibrations below 350 cm-1". In: *The Journal of Chemical Physics* 134, p. 104506. DOI: 10.1063/1.3551620.

Acharya, Y.B., Som Sharma, and H. Chandra (2004). "Signal induced noise in PMT detection of lidar signals". In: *Measurement* 35, pp. 269–276. DOI: 10.1016/j.measurement.2003.11.003.

Allen, Wesley D. et al. (1990). "A systematic study of molecular vibrational anharmonicity and vibration-rotation interaction by self-consistent-field higher-derivative methods. Linear polyatomic molecules". In: *Chemical Physics* 145, pp. 427–466. DOI: 10.1016/0301-0104(90)87051-C.

Alluxa (2024). *Temperature Dependence of Optical Filters*. Accessed: 2024-08-23. URL: https://alluxa.com/optical-filter-specs/temperature-dependence/.

Althausen, Dietrich et al. (2009). "Portable Raman Lidar PollyXT for Automated Profiling of Aerosol Backscatter, Extinction, and Depolarization". In: *Journal of Atmospheric and Oceanic Technology* 26.11, pp. 2366–2378. DOI: 10.1175/2009JTECHA1304.1. URL: https://journals.ametsoc.org/view/journals/atot/26/11/2009jtecha1304_1.xml.

Ansmann, A. and D. Müller (2005). "Lidar and Atmospheric Aerosol Particles". In: *Lidar*. Ed. by C. Weitkamp. Vol. 102. Springer Series in Optical Sciences. New York, NY: Springer, pp. 105–141. DOI: 10.1007/0-387-25101-4_4.

Aschi, Massimiliano et al. (2005). "Theoretical Characterisation of the Electronic Excitation in Liquid Water". In: *ChemPhysChem* 6.1, pp. 53–58. DOI: 10.1002/cphc.200400265.

Azzam, R. M. A. (1985). "Variable-reflectance thin-film polarization-independent beam splitters for 0.6328- and 10.6-μm laser light". In: *Optics Letters* 10.3, pp. 110–112. DOI: 10.1364/OL.10.000110.

Baars, H., A. Ansmann, et al. (2012). "Aerosol profiling with lidar in the Amazon Basin during the wet and dry season". In: *Journal of Geophysical Research: Atmospheres* 117. DOI: 10.1029/2012JD018338.

Baars, H., R. Engelmann, et al. (2023). *Active Remote Sensing with Lidar*. Course Material, Leibniz Institute for Tropospheric Research (TROPOS).

Banwell, C. N. and Elaine M. McCash (1994). *Fundamentals of Molecular Spectroscopy*. McGraw-Hill. URL: http://www.rnlkwc.ac.in/pdf/study-material/chemistry/Spectroscopy.pdf.

Bass, Michael, ed. (2010). *Handbook of Optics: Volume I - Geometrical and Physical Optics, Polarized Light, Components and Instruments*. 3rd. New York:

McGraw-Hill Professional. URL: https://www.accessengineeringlibrary.com/content/book/9780071498890.

Behrendt, A. (2005). "Temperature Measurements with Lidar". In: *Lidar*. Ed. by C. Weitkamp. Vol. 102. Springer Series in Optical Sciences. Springer, New York, NY, pp. 273–305. DOI: 10.1007/0-387-25101-4_10.

Buenker, Robert J. et al. (2000). "Theoretical study of the electronic structure of carbon dioxide: Bending potential curves and generalized oscillator strengths". In: *Journal of Chemical Physics* 113, pp. 1046–1054. DOI: 10.1063/1.481884.

Collis, Ronald T. H. (1965). "Lidar Observation of Cloud". In: *Science* 149.3687, pp. 978–981. DOI: 10.1126/science.149.3687.978.

Elterman, L. (1968). "UV, Visible, and IR Attenuation for Altitudes to 50 km". In: *Environmental Research Papers* 285, pp. 1–49. URL: https://apps.dtic.mil/sti/tr/pdf/AD0671933.pdf.

Engelmann, Ronny et al. (2018). "Measurements of particle backscatter, extinction, and lidar ratio at 1064 nm with the rotational raman method in Polly-XT". In: *EPJ Web Conf.* 176. DOI: 10.1051/epjconf/201817601004. URL: https://doi.org/10.1051/epjconf/201817601004.

Griesche, Hannes et al. (July 2021). "Contrasting ice formation in Arctic clouds: Surface-coupled vs. surface-decoupled clouds". In: *Atmospheric Chemistry and Physics* 21, pp. 10357–10374. DOI: 10.5194/acp-21-10357-2021.

Hahn, David W. (2009). *Light Scattering Theory*. Department of Mechanical and Aerospace Engineering. URL: http://plaza.ufl.edu/dwhahn/Rayleigh%20and%20Mie%20Light%20Scattering.pdf.

Hecht, Eugene (2017). *Optics*. 5th Edition. Pearson. ISBN: 978-0133977226.

Hopkins, J. L. (1991). "Dead Time". In: *International Amateur-Professional Photoelectric Photometry Communication* 46, p. 9.

Koonen, T. (2006). "Fabry-Perot Interferometer Filters". In: *Wavelength Filters in Fibre Optics*. Ed. by H. Venghaus. Vol. 123. Springer Series in Optical Sciences. Springer. DOI: 10.1007/3-540-31770-8_7.

Lehr, C. G. (1966). "Satellite Tracking with a Laser". In: *SAO Special Report* 215, pp. 1–52. URL: https://adsabs.harvard.edu/full/1966SAOSR.215.....L.

Lovas, Frank J., J. S. Coursey, et al. (2003). *Triatomic Spectral Database*. NIST Standard Reference Database 117, NIST Physical Measurement Laboratory, Last Updated: July 2003. National Institute of Standards and Technology (NIST). DOI: 10.18434/T4DW2S.

Lovas, Frank J., Eberhard Tiemann, et al. (2005). *Diatomic Spectral Database*. NIST Standard Reference Database 114, NIST Physical Measurement Laboratory, Last Updated: November 2005. National Institute of Standards and Technology (NIST). DOI: 10.18434/T4T59X.

Ludwig, Juliane (2014). "LIDAR measurements: Determination of the aerosol extinction coefficient and comparison of incomplete overlap correction methods". Meteorological Institute Munich. Master Thesis. Ludwig-Maximilians-Universität München.

Macleod, H. Angus and Zoran Milanovic (1992). "Immersed beamsplitters - an old problem". In: *Optical Interference Coatings 1992, Optical Interference Coatings Technical Digest Series*. Optica Publishing Group. DOI: 10.1364/OIC.1992.OMB6.

Maiman, T. H. (1960). "Stimulated optical radiation in ruby". In: *Nature* 187, pp. 493–494. DOI: 10.1038/187493a0.

Newport Corporation (2024). *Broadband Dielectric Beamsplitters*. https://www.newport.com/f/broadband-dielectric-beamsplitters. Accessed: 2024-08-23.

NIST Chemistry WebBook (2023). NIST Standard Reference Database Number 69, Last Updated: 2023. National Institute of Standards and Technology (NIST). DOI: 10.18434/T4D303.

NIST Computational Chemistry Comparison and Benchmark Database (2022). NIST Standard Reference Database Number 101, Release 22, May 2022, Editor: Russell D. Johnson III. National Institute of Standards and Technology (NIST). DOI: 10.18434/T47C7Z.

Placzek, G. (1934). "The Rayleigh and Raman scattering". In: *Handbuch der Radiologie* 6.

Salvadé, Yves et al. (Sept. 2002). "Air-dispersion measurement by second-harmonic heterodyne interferometry". In: *Optics letters* 27, pp. 1424–6. DOI: 10.1364/OL.27.001424.

TROPOS (2024a). *Doku Wiki*. URL: https://wiki.tropos-rsd.de (visited on 08/23/2024).

— (2024b). *PollyNET - Coordinated Observations and Networks*. URL: https://polly.tropos.de (visited on 08/23/2024).

Veselovskii, I. et al. (2015). "Use of rotational Raman measurements in multiwavelength aerosol lidar for evaluation of particle backscattering and extinction". In: *Atmospheric Measurement Techniques* 8.8, pp. 4111–4122. DOI: 10.5194/amt-8-4111-2015.

Wandinger, U. (2005a). "Introduction to Lidar". In: *Lidar*. Ed. by C. Weitkamp. Vol. 102. Springer Series in Optical Sciences. Springer, New York, NY, pp. 1–18. DOI: 10.1007/0-387-25101-4_1.

— (2005b). "Raman Lidar". In: *Lidar*. Ed. by C. Weitkamp. Vol. 102. Springer Series in Optical Sciences. Springer, New York, NY, pp. 241–271. DOI: 10.1007/0-387-25101-4_9.

Wandinger, Ulla and Albert Ansmann (2002). "Experimental determination of the lidar overlap profile with Raman lidar". In: *Applied Optics* 41.3, pp. 511–514. DOI: 10.1364/ao.41.000511.

Wilson, Edgar Bright, J. C. Decius, and Paul C. Cross (1980). *Molecular Vibrations: The Theory of Infrared and Raman Vibrational Spectra*. Unabridged, Revised Edition. Dover Books on Chemistry. Courier Corporation, p. 388.

Woodward, J. H. and E. B. Walters (1971). *Laser altimeter for Apollo lunar orbit*. Tech. rep. NASA. URL: https://ntrs.nasa.gov/citations/19720032120.

Yang, Guangning et al. (1997). "Temporal characteristics of narrow-band optical filters and their application in lidar systems". In: *Optics Letter* 22, pp. 414–416. DOI: 10.1364/OL.22.000414.

Selbstständigkeitserklärung

Ich, Nathan Skupin, versichere, dass ich die vorliegende Arbeit selbstständig und ohne unerlaubte Hilfe angefertigt habe und dass ich andere als die angegebenen Quellen nicht benutzt habe. Die den benutzten Quellen wörtlich oder inhaltlich entnommenen Stellen wurden als solche kenntlich gemacht habe. Das gilt auch für sämtliche Abbildungen.
Die eingereichte Arbeit ist weder vollständig noch in wesentlichen Teilen Gegenstand eines anderen Prüfungsverfahrens gewesen.
Darüber hinaus versichere ich, dass die elektronische Version der Arbeit mit der gedruckten Version übereinstimmt.

Leipzig, den 3. September

Unterschrift: _____